

1 Nitrous Acid Budgets in Coastal Atmosphere: Potential Daytime Marine Sources

2 Xuelian Zhong¹, Hengqing Shen^{1*}, Min Zhao¹, Ji Zhang¹, Yue Sun¹, Yuhong Liu¹, Yingnan Zhang¹,
3 Ye Shan¹, Hongyong Li¹, Jiangshan Mu¹, Yu Yang¹, Yanqiu Nie¹, Jinghao Tang², Can Dong¹, Xinfeng
4 Wang¹, Yujiao Zhu¹, Mingzhi Guo², Wenxing Wang¹, and Likun Xue^{1*}

5 ¹Environment Research Institute, Shandong University, Qingdao, Shandong, 266237, China

6 ²Collage of Mechanics and Materials, Hohai University, Nanjing, Jiangsu, 210098, China

7 *Correspondence to* Hengqing Shen (hqshen@sdu.edu.cn) and Likun Xue (xuelikun@sdu.edu.cn)

8 9 **Abstract.**

10 Nitrous acid (HONO), a vital precursor of atmospheric hydroxyl radicals (OH), has been extensively
11 investigated to understand its characteristics and formation mechanisms. However, discerning
12 fundamental mechanisms across diverse environments remains challenging. This study utilizes
13 measurements from Mount Lao, a coastal mountain in eastern China, and an observation-based
14 chemical box model (OBM) to examine HONO budgets and their subsequent impacts on atmospheric
15 oxidizing capacity. The model incorporates additional HONO sources, including direct emissions,
16 heterogeneous conversions of NO₂ on aerosol and ground surfaces, and particulate nitrate photolysis.
17 The observed mean HONO concentration was 0.46 ± 0.37 ppbv. The updated model well reproduced
18 daytime HONO concentrations during dust and photochemical pollution events. During dust events,
19 daytime HONO formation was dominated by photo-enhanced heterogeneous reactions of NO₂ on
20 aerosol surfaces (>50%), whereas particulate nitrate photolysis (34%) prevails during photochemical
21 pollution events. Nevertheless, the model uncovers a significant unidentified marine HONO source in
22 the “sea case”, with its HONO production rate reaching up to 0.70 ppbv h⁻¹ at noon. Without
23 considering this unidentified source, an extraordinarily high photolysis coefficient of nitrate and/or
24 heterogeneous uptake coefficient of NO₂ would be required to match observed HONO concentrations.
25 This missing marine HONO source affected the peak O₃ production rate and OH radical concentration
26 by 36% and 28%, respectively, at the observation site. Given the limited HONO observation data in
27 coastal and marine settings, the unidentified HONO source may cause an underestimation of the
28 atmosphere’s oxidizing capacity. This study highlights the necessity for further investigation of the
29 role of HONO in atmospheric chemistry in coastal and marine environments.

31 **1 Introduction**

32 Atmospheric nitrous acid (HONO) serves as a pivotal precursor of hydroxyl radicals (OH) ([Alicke](#)
33 [et al., 2003](#)), accounting for up to 60% of daytime OH radicals ([Kleffmann et al., 2005](#); [Czader et al.,](#)
34 [2012](#)). Thus, HONO establishes itself as a critical source of OH radical source in both urban and rural
35 environments, surpassing the contribution from ozone (O₃) photolysis ([Acker et al., 2006](#); [Elshorbany](#)
36 [et al., 2012](#); [Gu et al., 2022a](#)). Consequently, HONO substantially influences the formation of
37 secondary pollutants, including secondary aerosols and O₃, exerting a considerable effect on air quality
38 and climate change ([Xing et al., 2019](#); [Yang et al., 2021b](#)).

39 Recent studies pinpoint four primary sources of atmospheric HONO: (a) Direct emissions from
40 traffic ([Liao et al., 2021](#)), biomass burning ([Nie et al., 2015](#); [Theys et al., 2020](#)), soil ([Su et al., 2011](#)),
41 and livestock farming ([Zhang et al., 2023](#)). (b) Homogeneous reaction of NO + OH, which is generally
42 regarded as a significant process in polluted urban areas during daytime when NO and OH
43 concentrations are relatively high ([Gu et al., 2022a](#)). (c) Heterogeneous reactions of NO₂ on various
44 surfaces, such as mineral dust ([Underwood et al., 2001](#)), soil ([Kebede et al., 2016](#)), and aqueous
45 surfaces ([Wojtal et al., 2011](#)). The uptake coefficient of NO₂, $\gamma(\text{NO}_2)$, on these surfaces remains
46 uncertain and is subject to varying factors, sparking debates regarding the importance of the
47 heterogeneous conversion of NO₂ ([Broske et al., 2003](#); [Xue et al., 2022](#)). (d) Photolysis of adsorbed
48 nitric acid (HNO₃) and particulate nitrate (pNO₃⁻), crucial contributors to daytime HONO formation
49 ([Ye et al., 2017](#); [Gen et al., 2022](#)), particularly in clean environments ([Zhou et al., 2011](#); [Ye et al.,](#)
50 [2016a](#)). However, HONO formation mechanisms in different environments remain contentious and
51 require more detailed model evaluations ([Jiang et al., 2022](#)).

52 Despite its short daytime atmospheric lifetime, HONO is frequently observed at high
53 concentrations at noon ([Ye et al., 2016a](#); [Yang et al., 2021a](#); [Jiang et al., 2023](#)). Traditional mechanisms
54 cannot fully explain these observed daytime HONO peaks, indicating the presence of additional
55 daytime HONO sources (missing sources of daytime HONO). Over recent decades, researchers have
56 extensively investigated the missing sources of daytime HONO in various environments ([Kleffmann,](#)
57 [2007](#); [Lee et al., 2016](#); [Jiang et al., 2022](#); [Zhang et al., 2022](#)). However, our limited understanding of
58 these unidentified HONO sources has hindered accurate assessments of atmospheric free radicals and
59 oxidizing capacity ([Tang et al., 2015](#)). In areas with high concentrations of NO₂ and particulate matter,
60 missing sources are often ascribed to the photolytic enhancement of heterogeneous NO₂ reactions ([Su](#)
61 [et al., 2008](#); [Czader et al., 2012](#); [Lee et al., 2016](#); [Tong et al., 2016](#)), which also can be intensified by
62 the presence of other substances (e.g., ammonia or sulfur dioxide) ([Ma et al., 2017](#); [Li et al., 2018b](#);
63 [Ge et al., 2019](#)). Conversely, in remote areas, nitrate photolysis or soil emissions are perceived as

64 significant contributors to daytime HONO sources ([Su et al., 2011](#); [Ye et al., 2016a](#); [Cui et al., 2019](#)).
65 In polluted mountainous areas, the vertical transport of air masses may also contribute to observed
66 daytime HONO concentrations ([Jiang et al., 2020](#); [Xue et al., 2022](#)). During dust storms, the particle
67 surface area increases sharply, potentially enhancing the heterogeneous reaction of NO₂, yet the
68 evaluations of dust impacts on daytime HONO are scarce ([Wang, 2003](#)). Overall, most existing HONO
69 source studies lack quantitative assessments based on models and fail to provide comparative analyses
70 across different environmental scenarios.

71 The marine boundary layer (MBL) with a large air/water interface, where the ocean and
72 atmosphere exchange trace gases, heat, and aerosol particles ([Wurl et al., 2016](#)), and the interfacial
73 photochemistry processes often occur ([Bruggemann et al., 2018](#)), is utterly different from inland
74 environments. The opposite diurnal variations of HONO with a peak concentration at noon at marine
75 sites implied the different predominant HONO processes compared with polluted inland areas ([Jiang
76 et al., 2022](#)). Furthermore, recent observations of HONO in coastal and marine regions indicate the
77 existence of marine HONO sources ([Ye et al., 2016a](#); [Crilley et al., 2021](#); [Yang et al., 2021a](#); [Jiang et
78 al., 2022](#)). The observed accelerated NO₂-to-HONO conversion in marine air masses suggests that air-
79 marine interactions enhance HONO production ([Zha et al., 2014](#); [Yang et al., 2021a](#)). However, the
80 heterogeneous conversion of NO₂ on vast air/water interface, a potential source of marine HONO,
81 remains uncertain ([Wojtal et al., 2011](#); [Yu et al., 2021](#); [Zhu et al., 2022](#)). [Crilley et al. \(2021\)](#) only
82 obtained a factor of 5 lower ocean-surface NO₂-to-HONO conversion than previous studies; there was
83 still a debate on the importance of ocean-surface-mediated conversion of NO₂ into HONO. Nitrate
84 photolysis is believed to contribute to marine HONO sources ([Ye et al., 2016a](#); [Andersen et al., 2023](#)),
85 but significant controversy persists ([Romer et al., 2018](#); [Shi et al., 2021](#)). The specific influencing
86 factors remain unclear ([Zhang et al., 2020](#); [Andersen et al., 2023](#)), with some studies suggesting other
87 factors may be responsible ([Wojtal et al., 2011](#); [Yang et al., 2021a](#)). [Accordingly, Jiang et al. \(2023\)](#)
88 highlighted the contribution of the dust-surface-photocatalytic conversion of reactive nitrogen
89 compounds to HONO formation and the important role of halogen chemistry in HONO simulation in
90 CVAO. However, most existing studies still rely on steady-state analysis, and there is a lack of
91 quantitative research determining if current HONO mechanisms can adequately explain observed
92 marine daytime HONO concentrations.

93 Mount Lao, located on the eastern coast of Qingdao, China, experiences influences from various
94 air masses from the continent and the ocean. During the spring of 2021 (27 April–19 May), when dust
95 and O₃ pollution occurred frequently, we conducted measurements on Mount Lao to explore the
96 daytime HONO budgets in the coastal atmosphere. Utilizing the latest HONO formation mechanisms

97 in the box model, we found that the existing parameters adequately accounted for the HONO sources
98 during both dust and photochemical pollution periods. However, we identified a significant
99 discrepancy between the simulated and observed HONO in the “sea case”. This discrepancy suggests
100 that a substantial daytime source of marine-derived HONO is absent from the current chemical
101 mechanisms. To compensate for this missing source, either an unprecedentedly large enhancement
102 factor (EF) of nitrate photolysis or a heterogeneous uptake coefficient of NO₂ would be necessary if
103 attributed solely to these known HONO sources.

104 **2 Methods**

105 **2.1 Field measurements**

106 Field measurements were conducted on the southeast coast of Mount Lao (36.15°N, 120.68°E,
107 166 m above sea level) in Qingdao (Figure 1), approximately 1 km away from the Yellow Sea. The
108 geographical location and elevation of Mount Lao make it an optimal location for examining the
109 contrasts between marine and continental air masses and the chemical processes within the marine
110 boundary layer. The relatively pristine condition of the area, coupled with minimal levels of
111 anthropogenic activities such as industrial emissions, establish Mount Lao as a representative of a
112 clean environment. The field campaign was carried out during the spring of 2021 (27 April–19 May
113 2021), a period when the air quality of Qingdao is often affected by dust storms from Mongolia and
114 northwestern China, as well as by O₃ pollution. Consequently, the site at Mount Lao provides an
115 opportune platform for investigating the fundamental formation mechanisms of HONO under diverse
116 environmental conditions.

117 HONO was quantified using a water-based long-path absorption photometer (WLPAP, Beijing
118 Zhichen Technology Co., Ltd, China). Ambient HONO was absorbed by deionized water alone, after
119 which it reacted with a reagent comprising 3.44 g of sulfanilamide and 0.2 g of N-(1-naphthyl)-
120 ethylenediamine-dihydrochloride (NED) in 10 liters of deionized water, leading to the formation of an
121 azo dye. Two channels were employed to extract HONO and interfering gases, respectively. The
122 absorbance of the azo dye was measured using a fiber optic spectrometer (USB 4000, Ocean Optics,
123 USA) at both the measurement wavelength (550 nm) and the reference wavelength (580 nm). Regular
124 automatic zero measurements using ultrapure nitrogen were conducted every two days to correct for
125 baseline drift. The detection limit and detection ranges were 2 pptv and 5 pptv–2 ppmv, respectively.

126 A suite of commercial online analyzers monitored the concentrations of NO_x, O₃, SO₂, and CO
127 (42i, 49i, 43i, and 48i, respectively, Thermo Fisher Scientific Inc, USA). PM_{2.5} was measured using a
128 hybrid nephelometric/radiometric particulate mass monitor (SHARP-5030i, Thermo Fisher Scientific

129 Inc, USA), while PM₁₀ mass data were obtained from the China National Environmental Monitoring
130 Center (<https://quotsoft.net/air/>). During the field campaign, fifty-seven VOC (volatile organic
131 compound) canister samples were collected at 2-hour intervals from 9:00–19:00 local time on pollution
132 episode days and at 6-hour intervals from 9:00–21:00 on non-episode days. These VOC samples were
133 subsequently analyzed using gas chromatography and mass spectrometry (TT24xr, Markes, UK; GC–
134 MS, Thermo Fisher Scientific Inc, USA) (Liu et al., 2021). A wide-range particle spectrometer (WPS,
135 Model 1000XP, MSP, USA) was employed to determine the atmospheric particle number size
136 distributions from 10 nm to 10 μm. Taking into account the hygroscopic growth, the relative humidity-
137 adjusted aerosol surface area concentration (Sa) was calculated based on the determined particle
138 number size distributions. 95 offline particulate samples were collected every 3-hour interval from
139 7:00–19:00 and 12-hour intervals from 19:00–7:00 utilizing a high-volume air-sampling system (TE-
140 5170, Tisch Environmental Inc, USA). The inorganic compositions of the samples, including Cl⁻, NO₃⁻,
141 SO₄⁻, NH₄⁺, Na⁺, K⁺, Mg²⁺, and Ca²⁺, were determined via ion chromatography (Dionex ICS-600,
142 Thermo Fisher Scientific Inc, USA). Meteorological data, including temperature, RH, pressure, wind
143 speed, and wind direction, were monitored by an ultrasonic integrated weather station (RS-FSXCS-
144 N01-1).

145 This study distinguishes between the “sea case” and the “land case” by analyzing the backward
146 trajectory of the air mass. Specifically, considering the short lifetime of HONO, the MeteoInfo model
147 (Wang, 2012) was used to calculate 6-hour air mass backward trajectories starting at the height of 200
148 meters above ground level, using meteorological parameters from the Global Data Assimilation
149 System (GDAS, <ftp://arlftp.arlhq.noaa.gov/>). The criteria for differentiating between the “sea case”
150 and “land case” is based on the time spent over land or sea during the 6-hour backward air mass, with
151 cases that spent less than 1 hour over land designated as a “sea case” (Yang et al., 2021a). Following
152 this criterion, we selected a total of 18 sea cases and 13 land cases (Table S1). The observation data
153 for the “sea case” and the “land case” were averaged for subsequent analysis.

154 2.2 Model setup

155 An observation-based chemical box model (OBM) was employed to explore the HONO budgets
156 and atmospheric oxidizing capacity. The chemical mechanism used for the modeling was obtained
157 from the Master Chemical Mechanism (MCM) website (<http://mcm.york.ac.uk/>) and was based on the
158 MCM v3.3.1 as proposed by Jenkin et al. (2015). The model was constrained with data including
159 HONO, O₃, NO, NO₂, SO₂, CO, VOCs, pNO₃⁻, Sa, temperature, RH, pressure, and JNO₂. The
160 observed data of HONO, O₃, NO, NO₂, SO₂, CO, VOCs, pNO₃⁻, Sa, temperature, RH, and pressure
161 were averaged or interpolated to a time resolution of 5 minutes, except for VOCs and pNO₃⁻, which

162 were linearly interpolated to a time resolution of 1 hour to constrain the model (Yang et al., 2018). The
163 calculation of the photolysis rate of NO₂, JNO₂, was determined using Equation 1:

$$JNO_2 = JNO_{2(TUV)} \times \frac{UV_{observed}}{UV_{TUV}} \quad (E1)$$

164 where JNO_{2(TUV)} and UV_{TUV} are obtained from the Tropospheric Ultraviolet and Visible (TUV)
165 radiation model (http://cprm.acom.ucar.edu/Models/TUV/Interactive_TUV/). The UV_{observed} was
166 obtained from the NASA GES DISC (<https://disc.gsfc.nasa.gov/>). Other photolysis frequencies were
167 calculated in the OBM and scaled by JNO₂. The time series of JNO₂ is presented in Figure S1. The
168 model was pre-run for 1 day to stabilize the simulation of unconstrained species.

169 In the MCM v3.3.1, the formation of HONO is originally attributed to a homogeneous reaction,
170 specifically NO + OH → HONO. This study extends the existing mechanism by incorporating
171 additional sources of HONO into the chemical model. A description of these sources and their
172 associated mechanisms is provided in the following, and the corresponding parameters are listed in
173 Table 1.

174 **Description of HONO sources and sinks adopted in the OBM**

175 **Direct emission**

176 In the atmosphere, HONO can be directly released through the exhaust emissions of various sources.
177 The HONO/NO_x emission ratio, which typically averages around 0.8%, is a common parameter used
178 to gauge the impact of these vehicular emissions on HONO concentration (Kleffmann et al., 2003;
179 Czader et al., 2012; Lee et al., 2016; Xue et al., 2020a). However, the ratio can fluctuate between 0.3%
180 and 1.6%, depending on engine and fuel types (Kurtenbach et al., 2001). Prior research indicates that
181 direct emissions contribute significantly to HONO concentration in urban settings (Zhang et al., 2019;
182 Kramer et al., 2020). However, in rural and background areas, the vehicular contribution is
183 comparatively insignificant (Liu et al., 2019b; Xue et al., 2022). Consequently, the contribution of
184 vehicle emissions to HONO is not constant and varies based on the environment and traffic density.
185 In this study, we employed the widely used ratio of 0.8% for modeling scenarios and sensitivity
186 simulations using ratios of 0.4% and 1.6%.

187 **Homogeneous reaction of OH + NO → HONO**



188 The reaction of NO + OH is considered an important gas-phase reaction for HONO formation,
189 particularly during pollution periods when concentrations of NO and OH are high (Gu et al., 2022a).

190 We employed the box model to calculate the reaction rate using complex rate coefficients from the
 191 MCM website (<http://mcm.york.ac.uk/parameters/complex.htm>).

192 Heterogeneous reaction of NO₂ on aerosol surfaces



$$k_{\text{aerosol}} = 0.25 \times v_{\text{NO}_2} \times \text{Sa} \times \gamma_a \quad \gamma_a = 8 \times 10^{-6} \quad (\text{E2})$$

$$k_{\text{aerosol}, h\nu} = 0.25 \times v_{\text{NO}_2} \times \text{Sa} \times \gamma_{a, h\nu} \times \frac{J_{\text{NO}_2}}{J_{\text{NO}_2, \text{noon}}} \quad \gamma_{a, h\nu} = 4 \times 10^{-5} \quad (\text{E3})$$

$$v_{\text{NO}_2} = \sqrt{\frac{8RT}{\pi M}} \quad (\text{E4})$$

193 The heterogeneous conversion of NO₂ on surfaces is a significant source of HONO in the atmosphere.
 194 As illustrated by equations R2 and R3, NO₂ reacts with water and light on aerosol surfaces to produce
 195 HONO. The HONO formation rate from heterogeneous reactions is typically first-order with respect
 196 to NO₂ concentration ([Aumont et al., 2003](#)), and the reactivity of NO₂ is known to be significantly
 197 enhanced under irradiated conditions compared to darkness ([Yu et al., 2022a](#)). In this study, the uptake
 198 coefficients of NO₂ on the aerosol surface in dark and irradiated conditions, γ_a and $\gamma_{a, h\nu}$, were set to
 199 8×10^{-6} and 4×10^{-5} ([Lelièvre et al., 2004](#); [Vandenboer et al., 2013](#)), respectively. The molecular speed
 200 of NO₂ (v_{NO_2} , m s⁻¹) was calculated using Equation 4, where R represents the ideal gas constant, 8.314
 201 J mol⁻¹ K⁻¹, T is the absolute temperature (K), and M is the relative molecular weight of NO₂ (g mol⁻¹
 202 ¹). Sa is the surface area concentration (m² m⁻³) estimated from particle number concentrations
 203 measured by the WPS.

204 Heterogeneous reaction of NO₂ on ground surfaces



$$k_{\text{ground}} = 0.25 \times v_{\text{NO}_2} \times \gamma_g \times \frac{S}{V} \quad \gamma_g = 1 \times 10^{-6} \quad (\text{E5})$$

$$k_{\text{ground}, h\nu} = 0.25 \times v_{\text{NO}_2} \times \gamma_{g, h\nu} \times \frac{S}{V} \times \frac{J_{\text{NO}_2}}{J_{\text{NO}_2, \text{noon}}} \quad \gamma_{g, h\nu} = 2 \times 10^{-5} \quad (\text{E6})$$

$$\frac{S}{V} = \frac{1.7}{\text{BLH}} \quad (\text{E7})$$

205 Equations 5 and 6 delineate the parameterizations for the heterogeneous reaction of NO₂ on the ground
 206 surfaces, both in the absence and presence of light. The uptake coefficients of NO₂ on the ground
 207 surface under dark and irradiated conditions, γ_g and $\gamma_{g, h\nu}$, respectively, were set to 1×10^{-6} and 2×10^{-5}
 208 ([Kleffmann et al., 1998](#); [Stemmler et al., 2006](#)), respectively. Under ambient conditions, the relative

209 importance of gas uptake on ground and aerosol surfaces is uncertain, with the influence of land use
 210 categories and chemical compositions (Li et al., 2019). The surface-to-volume ratio, $\frac{S}{V}$, is calculated
 211 by an effective surface of 1.7 m² per geometric surface in Equation 7 (Vogel et al., 2003). Within the
 212 model, the boundary layer height, BLH, is projected to increase from 300 m at dawn to 1500 m at
 213 14:00 and then decrease back to 300 m at dusk (Xue et al., 2014).

214 **Photolysis of particulate nitrate**



$$k = \frac{J(\text{pNO}_3^-)}{J\text{HNO}_3, \text{noon}} \times J\text{HNO}_3(\text{MCM}) \quad (\text{E8})$$

215 In Equation 8, the photolysis rate constant of gaseous HNO₃ at noon, JHNO_{3,noon}, is chosen to be ~
 216 $7 \times 10^{-7} \text{ s}^{-1}$ based on previous studies (Ye et al., 2016b). JHNO_{3(MCM)} is calculated by the box model.
 217 Recent research has shown that the photolysis rate of particulate nitrate is significantly faster than that
 218 in the gas and aqueous phases (Zhou et al., 2003; Ye et al., 2016a). We adopt a median value of $8.3 \times 10^{-5} \text{ s}^{-1}$
 219 in our simulation based on a range provided by Ye et al. (2017). Considering the uncertainty of
 220 the parameter values of the above-mentioned HONO formation mechanisms, we conducted the
 221 sensitivity tests with lower and upper values in Sections 3.2 and 3.3.

222 **Photolysis of HONO**



223 The primary loss pathway of HONO is through photolysis following sunrise, which significantly
 224 contributes to the atmospheric OH budget. The photolysis rate of HONO, J(HONO), in the OBM, is
 225 constrained by JNO₂.

226 **Homogeneous reaction between HONO and OH**



227 The relevant kinetic parameter of the reaction between HONO and OH is available from the MCM
 228 mechanism, and its reaction rate coefficient is dependent solely on the temperature.

229 **Dry deposition of HONO**

$$k = \frac{v_{\text{HONO}}}{\text{BLH}} \quad (\text{E9})$$

230 Here, v_{HONO} is the dry deposition velocity of HONO (cm s⁻¹). Harrison and Kitto (1994) suggested the
 231 range of v_{HONO} was 0.2–1.7 cm s⁻¹, and a value of 1.0 cm s⁻¹ was employed in this study. **The dry**
 232 **deposition of HONO, ozone, and other species, including peroxides, carbonyls, and organic acids, are**
 233 **also considered in the OBM model (Xue et al., 2014).**

234 **3 Results and discussion**

235 **3.1 Concentration levels and temporal variations**

236 Figure 2 displays the time series of HONO, HONO/NO₂, NO_x, O₃, CO, SO₂, PM_{2.5}, and pNO₃⁻,
237 along with meteorological parameters (i.e., temperature, RH, and wind) measured throughout the field
238 campaign. The presence of missing data in the time series resulted from instrument maintenance and
239 calibration. Instrument maintenance and calibration resulted in gaps in the time series data. The
240 observation site underwent dust periods on April 27–28 and May 7–8, as well as periods of
241 photochemical pollution on May 5–6, 13, and 17–18. In this study, a photochemical pollution period
242 is classified as a day when the maximum daily 8-hour average O₃ concentration (MDA8O₃) exceeds
243 75 ppbv (the Grade II National Ambient Air Quality Standard). A dust period is recognized when the
244 peak PM₁₀ concentration surpasses 150 µg m⁻³, and the PM_{2.5}/PM₁₀ ratio falls below 0.4, based on
245 previous research ([Liu et al., 2006](#); [Wu et al., 2020](#)). Section 3.2 provides a comprehensive explanation
246 of the differences in pollutant concentrations and HONO budgets during dust and photochemical
247 pollution periods.

248 Table 2 summarizes the descriptive statistics of the species and meteorological parameters
249 measured during the observation period. The average (± standard deviation, SD) temperature and RH
250 were 15.1 ± 3.4 °C and 68.7 ± 26.1%, respectively, indicating a moderate spring temperature and
251 relatively high RH influenced by marine air masses. The primary pollutant concentrations were
252 relatively low, as indicated by the mean mixing ratios of 0.9 ± 1.7 ppbv, 5.9 ± 4.8 ppbv, 284.0 ± 118.8
253 ppbv, and 1.0 ± 0.8 ppbv for NO, NO₂, CO, and SO₂, respectively. These low levels suggest Mount
254 Lao is a relatively clean site with minimal impact from nearby anthropogenic sources. The high O₃
255 concentration (60.4 ± 15.8 ppbv) implies that photochemical reactions were relatively strong during
256 observation. The mean concentrations of PM_{2.5} and pNO₃⁻ were 21.2 ± 21.09 µg m⁻³ and 4.6 ± 5.0 µg
257 m⁻³, respectively.

258 During the campaign, the mean concentration of HONO was 0.46 ± 0.37 ppbv, with a maximum
259 mixing ratio of 3.14 ppbv recorded at 17:00 on May 4th. The concentration level of HONO at Mount
260 Lao is lower than at urban sites with higher NO₂ concentrations ([Li et al., 2018a](#); [Hao et al., 2020](#); [Yu
261 et al., 2022b](#)). However, it is notably higher than other clean coastal and remote marine sites, as Table
262 S2 illustrates ([Villena et al., 2011](#); [Zha et al., 2014](#); [Meusel et al., 2016](#); [Crilley et al., 2021](#); [Zhu et al.,
263 2022](#)). Past research conducted in urban and rural areas found that the HONO/NO₂ ratio, which
264 indicates the extent of NO₂ conversion to HONO, typically ranges from 0.02 to 0.08 ([Jiang et al., 2022](#)).

265 The higher HONO/NO₂ value (0.13) measured at Mount Lao highlights the potentially significant role
266 of non-NO_x related HONO sources or higher heterogeneous conversion of NO₂ efficiency at this site.

267 Figure 3 illustrates the average diurnal patterns of HONO and related species. The diurnal cycle
268 of CO and SO₂ is similar, with peak concentrations observed during midday and relatively stable
269 concentrations during nighttime. The concentration of O₃ increases with the accumulation of
270 photochemical generation during the afternoon and decreases steadily after sunset. Contrary to most
271 urban or rural locations, the concentration of HONO at Mount Lao peaks at noon, similar to remote
272 areas ([Ye et al., 2016a](#); [Jiang et al., 2022](#)). It is important to note that both HONO and NO_x exhibit a
273 second daytime peak in the late afternoon, primarily caused by specific days with relatively high
274 emissions or transport events. After excluding these days, the diurnal variation of HONO aligns more
275 closely with observations in clean regions ([Jiang et al., 2022](#)). We have included the diurnal variation
276 of HONO after removing days with afternoon peaks in the supporting information. Since their impact
277 is largely confined to specific days, it does not significantly affect our subsequent analysis, particularly
278 the “sea case” analysis. NO_x, comprising NO and NO₂, shows a similar temporal variation trend to
279 HONO, suggesting potential photolytic sources for them ([Reed et al., 2017](#)). During the daytime (7:00–
280 17:00), the average concentration of HONO was 1.56 times higher than at night (17:00–7:00), with
281 concentrations of 0.54 ppbv during the day and 0.35 ppbv at night. Given the short lifetime of HONO
282 during the day—only a matter of minutes—the noon HONO peak concentration suggests an in situ
283 photochemical source for HONO ([Kasibhatla et al., 2018](#)). The ratio of HONO to NO₂ shows an
284 increasing trend until sunrise, suggesting heterogeneous conversion from NO₂ to HONO during
285 nighttime. However, unlike urban areas where the ratio of HONO to NO₂ decreases during the daytime
286 ([Zhang et al., 2019](#); [Gu et al., 2022a](#)), the ratio even increases during the midday period at Mount Lao,
287 implying that HONO from sources other than NO₂ conversion also significantly contributes to HONO
288 concentration ([Yang et al., 2021a](#)). Considering that the influence of HONO on the OH radical and O₃
289 is primarily observed during the daytime, the higher concentration of HONO during the daytime at the
290 Mount Lao site suggests the presence of strong daytime HONO sources. The primary objective of our
291 following study is to analyze the daytime budgets of HONO in the coastal atmosphere of Mount Lao.

292 3.2 Daytime HONO budgets in dust and photochemical pollution periods

293 The daytime HONO budgets were examined during periods of dust and photochemical pollution
294 using an updated OBM, with the aim of assessing whether our current understanding of HONO sources
295 is sufficient to explain observed concentrations. Table 4 presents the mean daytime concentrations of
296 HONO and other species during the dust, photochemical pollution, and non-polluted periods (i.e., days
297 devoid of dust and photochemical pollution). On average, the daytime HONO concentrations during

298 dust and photochemical pollution periods were 0.57 ± 0.39 ppbv and 0.44 ± 0.29 ppbv, respectively.
299 The dust period exhibited significantly higher concentrations of NO_2 , $\text{PM}_{2.5}$, pNO_3^- , and Sa, with
300 increased factors of 1.4, 2.6, 2.3, and 2.3, respectively, compared to the non-polluted period. During
301 the photochemical pollution period, the daytime mean values of O_3 , CO, SO_2 , $\text{PM}_{2.5}$, pNO_3^- , and JNO_2
302 were 78.8 ppbv, 353.8 ppbv, 1.7 ppbv, $25.0 \mu\text{g m}^{-3}$, $6.2 \mu\text{g m}^{-3}$, and $7.0 \times 10^{-3} \text{ s}^{-1}$, respectively. These
303 values were approximately 1.4, 1.3, 2.4, 1.5, 2.1, and 1.6 times higher than those during the non-
304 polluted period.

305 Figure 4 compares the observed and modeled HONO concentrations during dust and
306 photochemical pollution periods and illustrates the contribution of various sources and sinks to the
307 HONO budget. The study examined two scenarios: the base case, which only considered the
308 homogeneous reaction $\text{NO} + \text{OH}$, and the model case, which considered all seven HONO sources
309 outlined in Table 1. The results indicated that the base case significantly underestimated the HONO
310 concentration, consistent with previous studies ([Liu et al., 2019b](#); [Zhu et al., 2022](#)). However, the
311 model case effectively replicated the observed HONO concentrations for both periods, even the high
312 noon concentrations. The index of agreement (IOA) values for HONO during the dust and
313 photochemical pollution periods were 0.96 and 0.88, respectively. This suggests that the updated
314 parameterization scheme employed in the model can adequately account for the observed HONO
315 concentrations at Mount Lao.

316 During the daytime, the average modeled production rates of HONO were 1.66 ppbv h^{-1} and 0.90
317 ppbv h^{-1} for the dust and photochemical pollution periods, respectively. The maximum HONO
318 production rate was significantly higher during the dust period (3.50 ppbv h^{-1}) compared to the
319 photochemical pollution period (1.69 ppbv h^{-1}) and was even comparable to levels observed during
320 haze periods at polluted urban or rural sites ([Zhang et al., 2019](#); [Xue et al., 2020b](#); [Gu et al., 2022a](#)).
321 Based on the model results of detailed HONO budgets, the dominant pathway for daytime HONO
322 production during the dust period was photo-enhanced heterogeneous conversion of NO_2 on the
323 aerosol surface, accounting for 53% ($0.87 \pm 0.66 \text{ ppbv h}^{-1}$) of the simulated daytime HONO production
324 rate. [Wang \(2003\)](#) reported sudden increases in HONO concentration during nocturnal dust storm
325 events and observed a higher ratio of HONO to NO_2 (0.18). The enhanced efficiency of NO_2 to HONO
326 on mineral dust particles suggests a potentially significant impact of dust aerosol on nitrogen
327 compound distribution. Further research is needed to understand the contribution of dust to HONO
328 formation and nitrogen cycling during the daytime, as well as its global impact. For the photochemical
329 pollution period, the major sources of HONO included the photolysis of particulate nitrate, the photo-
330 enhanced heterogeneous conversion of NO_2 on the aerosol surface, and the homogeneous reaction of

331 OH and NO, which contributed 34%, 27%, and 27% of the daytime HONO production rate,
332 respectively. This points to the significant role of photochemical processes under intense solar radiation.
333 Direct emissions had a negligible contribution during both the dust and photochemical pollution
334 periods, accounting for less than 2%. The photolysis of HONO was the dominant loss pathway
335 throughout the day for all measurement periods, accounting for more than 90% of HONO sinks.

336 The model was subjected to sensitivity tests by increasing or decreasing selected parameters by
337 factors of 5 and 2 (Table S4, Figures S3, and S4). Even with such a broad range of parameter variation,
338 the heterogeneous reaction of NO₂ on aerosols and the photolysis of nitrate to form atmospheric HONO
339 remained significant sources of HONO under both dust and photochemical pollution periods. This
340 suggests that our current understanding of HONO sources, based on existing mechanisms, can
341 generally explain the observed concentrations of HONO. However, it is important to note that
342 differences in parameter selection can significantly affect the relative contributions of each pathway.
343 Given the considerable uncertainties in the uptake coefficient of NO₂ and the enhancement factors of
344 photolysis of nitrate, further experimental studies are necessary to evaluate their effects on HONO in
345 different environmental conditions.

346 **3.3 Missing daytime HONO source in “sea case”**

347 Recent field studies suggest potential unidentified daytime sources of nitrous acid (HONO) in the
348 marine atmosphere, with high daytime HONO levels recorded ([Ye et al., 2016a](#); [Yang et al., 2021a](#)).
349 Figure 5 shows the diurnal variation of the selected “sea case” and “land case”, with corresponding
350 statistical results in Table S3. In the “sea case”, daytime concentrations of typical primary pollutants,
351 such as CO and SO₂, are significantly lower than those in the “land case” (251 ± 59 ppbv vs. $335 \pm$
352 115 ppbv and 0.7 ± 0.4 ppbv vs. 1.4 ± 0.8 ppbv for CO and SO₂, respectively). Concurrently, the “sea
353 case” shows a lower daytime temperature ($15.2 \pm 3.0^\circ\text{C}$ vs. $18.7 \pm 3.8^\circ\text{C}$) and higher RH ($76.3 \pm 25.9\%$
354 vs. $47.3 \pm 20.3\%$) compared to the “land case”. This is consistent with our understanding of marine air
355 masses, which tend to be cleaner and more humid. These findings validate our classification method
356 of “land case” and “sea case” based on the backward air mass trajectory.

357 Secondary pollutants in marine air masses, such as O₃, PM_{2.5}, and pNO₃⁻, also register lower
358 daytime concentrations than in the “land case” (59.4 ± 10.3 ppbv vs. 63.4 ± 13.3 ppbv, 13.2 ± 5.8 μg
359 m⁻³ vs. 29.9 ± 22.8 μg m⁻³, and 1.3 ± 0.5 μg m⁻³ vs. 10.0 ± 3.3 μg m⁻³, respectively). Though the
360 HONO concentration in marine air masses is less than that in the “land case” (0.42 ± 0.25 ppbv vs.
361 0.51 ± 0.22 ppbv), it maintains a relatively high level, particularly during intense photolysis periods
362 around noon when the HONO concentration in the “sea case” marginally increases. NO_x

363 concentrations in the “sea case” are also lower than in the “land case”, but the difference is less
364 substantial than primary pollutants, with both NO and NO₂ showing concentration peaks around noon.
365 Nighttime observations in the “sea case” show a higher HONO/NO₂ ratio (0.12), which has been noted
366 in earlier studies ([Zha et al., 2014](#)), suggesting strong nocturnal HONO formation in marine air masses.
367 Here, we focus on the sources of HONO during the day under the influence of marine air masses.

368 Utilizing the updated chemical model, we examine the HONO budgets in both “sea” and “land”
369 cases. In the “land case”, the simulated HONO concentration aligns well with the observed HONO
370 concentration, with a high index of agreement (IOA) value of 0.94 (Figure 6a). The peak HONO
371 production rate observed at Mount Lao (2.69 ppbv h⁻¹) surpasses that calculated in continental air
372 masses at Hok Tsui, Hong Kong (less than 1.5 ppbv h⁻¹) ([Gu et al., 2022b](#)). The contributions of photo-
373 enhanced heterogeneous reactions of NO₂ on the aerosol surface (22%) and photolysis of pNO₃⁻ (20%)
374 are comparable (Figure 6c). Model results reveal that the homogeneous reaction between NO and OH
375 is the predominant HONO formation pathway, contributing an average of 44% (0.52 ± 0.38 ppbv h⁻¹).
376 Despite a lower absolute rate than in urban areas, the relative contribution is significant([Gu et al.,](#)
377 [2022a](#); [Yu et al., 2022b](#)). This result suggests that similar to the findings in the cases of dust and
378 photochemical pollution, the current model’s parameterization reasonably accounts for the observed
379 HONO concentration in the “land case”.

380 However, in the “sea case”, while the updated model has improved in simulating HONO
381 concentrations, with an average concentration increase from 0.05 ppbv to 0.11 ppbv, it falls short of
382 the observed concentration (0.42 ppbv), indicating a substantial unidentified HONO source. At noon,
383 the missing HONO production rate (P_{missing}) can reach up to 0.70 ppbv h⁻¹. This value is slightly higher
384 than the result calculated by [Meusel et al. \(2016\)](#) on Cyprus Island (about 0.5 ppbv h⁻¹), but lower than
385 that reported by [Yang et al. \(2021a\)](#) in coastal Qingdao (up to 1.83 ppbv h⁻¹, including all non-NO+OH
386 pathways). Sensitivity tests were conducted to assess the impact of parameter selection on simulation
387 results, but even with much larger parameters (Table S4), the model fails to explain the observed
388 HONO concentrations (Figure S5).

389 The correlation analysis reveals that the missing HONO production rate correlates strongly with
390 JNO₂ and JNO₂×pNO₃⁻ (Figure S7), with correlation coefficients (r) of 0.90 and 0.73, respectively.
391 This indicates that the missing HONO sources are closely related to photochemical processes. This
392 concurs with recent multi-site HONO analysis results, which propose a significant role of
393 photochemical processes in observed HONO concentrations in remote areas ([Jiang et al., 2022](#)). We
394 postulate that all missing HONO originates from photochemical processes and have calculated the
395 required enhancement factors (EF) for nitrate photolysis rates (Text S2) and the uptake coefficient

396 required for NO₂ on aerosol and ground surfaces (Figure S6). To account for the observed HONO
397 concentrations, the required EF is approximately 4000. While [Andersen et al. \(2023\)](#) noted that the EF
398 increases with decreasing nitrate concentration, a 4000-fold difference exceeds all laboratory and field
399 observations to date ([Ye et al., 2017](#); [Andersen et al., 2023](#)). The required uptake coefficient of NO₂
400 on aerosol and ground surface reaches 4×10^{-4} , exceeding previous laboratory studies ([Stemmler et al.,](#)
401 [2007](#); [Liu et al., 2019a](#)). Although NO₂ uptake coefficients on the order of 10^{-4} have been measured
402 in laboratory experiments under conditions of high SO₂ concentration (280 ppbv) and moderate acidity
403 (pH = 5) ([Liu and Abbatt, 2021](#)), our observational site features lower SO₂ concentrations (~ 1 ppbv)
404 and slightly acidic aerosols (pH = 3.1). These conditions suggest that the uptake coefficients should
405 be considerably lower than the laboratory-measured 2×10^{-4} . It is worth noting that previous research
406 has indicated that the presence of halogens can enhance NO₂ uptake, which could potentially explain
407 the higher NO₂ to HONO conversion ratios in marine environments ([Yabushita et al., 2009](#)). However,
408 further research is needed to explore this possibility. Overall, the observed missing HONO source in
409 the “sea case” cannot be explained by the current photochemical processes. This deviates from the
410 findings of [Zhu et al. \(2022\)](#), who discovered that nitrate photolysis could explain the observed HONO
411 concentrations in clean marine air masses using a moderate EF of 29. In recent years, many
412 observations have noted distinct HONO characteristics under the influence of marine air masses,
413 differing from those in continental air masses, but the specific mechanisms are still lacking ([Meusel et](#)
414 [al., 2016](#); [Crilley et al., 2021](#); [Yang et al., 2021a](#); [Zhu et al., 2022](#)). The ocean surface contains
415 abundant nitrogen-containing substances (e.g., dissolved nitrate, ammonia, aliphatic amine, dissolved
416 free amino acids) ([Donaldson and George, 2012](#); [Altieri et al., 2016](#)), encompassing both organic and
417 inorganic nitrogen. This is particularly true in polluted coastal areas where surface nitrogen content is
418 rich. It merits investigation whether these nitrogen-containing substances in the alkaline sea-surface
419 microlayer can directly affect HONO production or enhance HONO formation by photolysis on the
420 formed sea salt aerosols. Additionally, the presence of halogens in oceanic air masses might promote
421 nitrate photolysis ([Zhang et al., 2020](#)).

422 3.4 Impacts of HONO on O₃ and OH production

423 To quantify the impact of HONO, especially in the marine atmosphere, on O₃ and OH radicals,
424 we conducted further scenario simulations using a chemical box model. In the “with HONO” scenario,
425 we input the observed HONO concentrations to constrain the model. In contrast, in the “without
426 HONO” scenario, we turn off seven HONO production pathways summarized in Table 1 and set the
427 input HONO concentrations to zero. The differences between these scenarios illustrate the impact of
428 HONO chemistry on O₃ and OH radicals in the atmosphere. To further investigate the effect of the

429 missing HONO sources in marine air masses, we established a third simulation scenario, “without
430 missing HONO”, in the marine air mass simulation. In this scenario, the model includes the latest
431 HONO formation mechanisms discussed earlier but without the constraint of observed HONO.

432 HONO significantly influences the production of O₃ and OH radicals, regardless of whether the
433 overall situation during the observation period (“overall case”) or the situation within the marine air
434 masses (“sea case”) is considered (Figure 7). The net O₃ production rate is determined by the difference
435 between the O₃ production rate (P(O₃)) and loss rate (L(O₃)) (Xue et al., 2014). Specifically, the
436 absence of HONO resulted in a decrease in the net O₃ production rate and OH radical primary
437 production rate in the “overall case” from 7.39 ppbv h⁻¹ and 1.44×10⁷ molecules cm⁻³ s⁻¹ to 3.41 ppbv
438 h⁻¹ (a 54% reduction) and 2.81×10⁶ molecules cm⁻³ s⁻¹ (an 81% reduction), respectively. Regarding
439 concentration, the absence of HONO chemistry resulted in a reduction in the average OH radical
440 concentration from 3.6×10⁶ molecules cm⁻³ to 1.9×10⁶ molecules cm⁻³, and the peak OH concentration
441 from 5.2×10⁶ molecules cm⁻³ to 2.7×10⁶ molecules cm⁻³. Similarly, in the marine air masses, the
442 production rates of O₃ and OH decreased from 6.22 ppbv h⁻¹ and 7.69×10⁶ molecules cm⁻³ s⁻¹ to 3.33
443 ppbv h⁻¹ (a 46% reduction) and 2.14×10⁶ molecules cm⁻³ s⁻¹ (a 72% reduction), respectively without
444 HONO chemistry. These findings are consistent with previous observational studies (Yang et al.,
445 2021a; Gu et al., 2022a), highlighting the significant impact of HONO on O₃ and OH radicals in the
446 atmosphere.

447 Notably, in the “sea case”, if the observed values are not input as constraints, and only the updated
448 mechanisms are used (“without missing HONO”), the model still significantly underestimates the
449 impact of HONO on O₃ and OH radicals. Specifically, missing marine HONO sources contributed 36%
450 to the peak net O₃ production rate (from 9.24 ppbv h⁻¹ to 5.90 ppbv h⁻¹) and 28% to peak OH
451 concentration (from 3.4×10⁶ molecules cm⁻³ to 2.4×10⁶ molecules cm⁻³). Regarding the relative
452 contribution to OH radicals, HONO accounts for 79% and 55% in the “overall case” and “sea case”,
453 respectively, both exceeding the combined contribution of other pathways (photolysis of O₃
454 contributes 14% and 25%, respectively). Given the relatively limited observational data on HONO in
455 coastal or marine areas and the unclear understanding of the missing HONO sources in the ocean, the
456 impact of marine emissions on atmospheric oxidizing capacity may be significantly underestimated.
457 This underscores the importance of further research in this area to enhance our understanding of the
458 role of HONO in atmospheric chemistry, especially in marine environments.

459 4 Conclusions

460 This study presents a comprehensive investigation of the characteristics and sources of nitrous
461 acid (HONO) in the coastal environment of Qingdao. The analysis utilizes observational data from the

462 Mount Lao site in Qingdao during spring 2021 and an updated chemical box model that integrates
463 HONO mechanisms. The focus lies on discerning the unidentified HONO sources in marine air masses
464 and comprehending their effects on atmospheric chemistry, emphasizing O₃ and OH concentrations.

465 Despite a relatively pristine coastal atmosphere, HONO concentrations are considerably higher
466 than previously thought (0.46 ± 0.37 ppbv), notably during daytime. This observation persists in lower
467 primary pollutant concentrations such as CO and SO₂ within marine air masses, suggesting missing
468 HONO sources tied to photochemical processes. An updated chemical model's simulation reveals that
469 the mechanisms behind HONO formation can satisfactorily account for the observed HONO
470 concentrations during the dust and photochemical pollution periods. Yet, in marine scenarios, the
471 model falls short of matching observed concentrations, pointing to a strong unidentified HONO source
472 within the marine atmosphere. Sensitivity tests and correlation analyses emphasize the importance of
473 photochemical processes in unidentified HONO sources. Nevertheless, if these unknown sources are
474 attributed to either nitrate photolysis or heterogeneous NO₂ reactions, the necessary nitrate photolysis
475 rate and the heterogeneous uptake coefficient of NO₂ would surpass the upper thresholds established
476 by current laboratory studies. In light of these findings, future research must target uncovering the
477 mechanisms behind the missing HONO sources in marine air masses. Specifically, the role of nitrogen-
478 containing substances at the ocean's surface and the potential influence of halogens in promoting
479 nitrate photolysis warrant further examination.

480

481 **Acknowledgments**

482 This work was supported by the National Science Foundation of China (grants nos. 42061160478 and
483 42105106) and the National Key Research and Development Programme of the Ministry of Science
484 of Technology of China (grant no. 2022YFC3701101). We would like to express our gratitude to the
485 University of Leeds for providing the Master Chemical Mechanism and to NCAR for the Tropospheric
486 Ultraviolet Visible (TUV) radiation model. We also thank Yaqiang Wang for developing the open-
487 source software MeteoInfo.

488 **Author contributing**

489 LX and HS conceptualized the research. XZ drafted the initial manuscript and analyzed the data. CD
490 supported funding the observation. YZ, CD, and XW designed the field campaign. MZ, JZ, YS, YL,
491 YS, HL, and JM conducted the field campaign. JZ and YL analyzed the aerosol samples and VOC
492 samples, respectively. MZ and YZ assisted with the model simulation. YY, YN, and JT contributed to
493 figure creation. LX, HS, MG, and WW revised the original manuscript.

494 **Competing interests**

495 The authors declare that they have no conflict of interest.

496 **Data availability**

497 The data supporting this study are available upon request from the corresponding author.

498

499 **References**

- 500 Acker, K., Möller, D., Wieprecht, W., Meixner, F. X., Bohn, B., Gilge, S., Plass-Dülmer, C., and
501 Berresheim, H.: Strong daytime production of OH from HNO₂ at a rural mountain site,
502 *Geophys. Res. Lett.*, 33, 4, [10.1029/2005gl024643](https://doi.org/10.1029/2005gl024643), 2006.
- 503 Alicke, B., Geyer, A., Hofzumahaus, A., Holland, F., Konrad, S., Pätz, H. W., Schäfer, J., Stutz, J.,
504 Volz-Thomas, A., and Platt, U.: OH formation by HONO photolysis during the BERLIOZ
505 experiment, *J. Geophys. Res. Atmos.*, 108, 8247, [10.1029/2001JD000579](https://doi.org/10.1029/2001JD000579), 2003.
- 506 Altieri, K. E., Fawcett, S. E., Peters, A. J., Sigman, D. M., and Hastings, M. G.: Marine biogenic source
507 of atmospheric organic nitrogen in the subtropical North Atlantic, *P. Natl. Acad. Sci.*, 113, 925-
508 930, [10.1073/pnas.1516847113](https://doi.org/10.1073/pnas.1516847113), 2016.
- 509 Andersen, S. T., Carpenter, L. J., Reed, C., Lee, J. D., Chance, R., Sherwen, T., Vaughan, A. R.,
510 Stewart, J., Edwards, P. M., Bloss, W. J., Sommariva, R., Crilley, L. R., Nott, G. J., Neves, L.,
511 Read, K., Heard, D. E., Seakins, P. W., Whalley, L. K., Boustead, G. A., Fleming, L. T., Stone,
512 D., and Fomba, K. W.: Extensive field evidence for the release of HONO from the photolysis
513 of nitrate aerosols, *Science Advances*, 9, [10.1126/sciadv.add6266](https://doi.org/10.1126/sciadv.add6266), 2023.
- 514 Aumont, B., Chervier, F., and Laval, S.: Contribution of HONO sources to the NO_x/HO_x/O₃ chemistry
515 in the polluted boundary layer, *Atmos. Environ.*, 37, 487-498, 2003.
- 516 Broske, R., Kleffmann, J., and Wiesen, P.: Heterogeneous conversion of NO₂ on secondary organic
517 aerosol surfaces: A possible source of nitrous acid (HONO) in the atmosphere?, *Atmos. Chem.*
518 *Phys.*, 3, 469-474, 2003.
- 519 Bruggemann, M., Hayeck, N., and George, C.: Interfacial photochemistry at the ocean surface is a
520 global source of organic vapors and aerosols, *Nat Commun*, 9, 2101, [10.1038/s41467-018-
521 04528-7](https://doi.org/10.1038/s41467-018-04528-7), 2018.
- 522 Crilley, L. R., Kramer, L. J., Pope, F. D., Reed, C., Lee, J. D., Carpenter, L. J., Hollis, L. D. J., Ball,
523 S. M., and Bloss, W. J.: Is the ocean surface a source of nitrous acid (HONO) in the marine
524 boundary layer?, *Atmos. Chem. Phys.*, 21, 18213-18225, [10.5194/acp-21-18213-2021](https://doi.org/10.5194/acp-21-18213-2021), 2021.
- 525 Cui, L. L., Li, R., Fu, H. B., Li, Q., Zhang, L. W., George, C., and Chen, J. M.: Formation features of
526 nitrous acid in the offshore area of the East China Sea, *Sci. Total Environ.*, 682, 138-150,
527 [10.1016/j.scitotenv.2019.05.004](https://doi.org/10.1016/j.scitotenv.2019.05.004), 2019.
- 528 Czader, B. H., Rappenglück, B., Percell, P., Byun, D. W., Ngan, F., and Kim, S.: Modeling nitrous
529 acid and its impact on ozone and hydroxyl radical during the Texas Air Quality Study 2006,
530 *Atmos. Chem. Phys.*, 12, 6939-6951, [10.5194/acp-12-6939-2012](https://doi.org/10.5194/acp-12-6939-2012), 2012.
- 531 Donaldson, D. J. and George, C.: Sea-Surface Chemistry and Its Impact on the Marine Boundary Layer,
532 *Environ. Sci. Technol.*, 46, 10385-10389, [10.1021/es301651m](https://doi.org/10.1021/es301651m), 2012.
- 533 Elshorbany, Y. F., Steil, B., Brühl, C., and Lelieveld, J.: Impact of HONO on global atmospheric
534 chemistry calculated with an empirical parameterization in the EMAC model, *Atmos. Chem.*
535 *Phys.*, 12, 9977-10000, [10.5194/acp-12-9977-2012](https://doi.org/10.5194/acp-12-9977-2012), 2012.
- 536 Ge, S., Wang, G., Zhang, S., Li, D., Xie, Y., Wu, C., Yuan, Q., Chen, J., and Zhang, H.: Abundant
537 NH₃ in China Enhances Atmospheric HONO Production by Promoting the Heterogeneous
538 Reaction of SO₂ with NO₂, *Environ. Sci. Technol.*, 53, 14339-14347, [10.1021/acs.est.9b04196](https://doi.org/10.1021/acs.est.9b04196),
539 2019.
- 540 Gen, M., Liang, Z., Zhang, R., Go Mabato, B. R., and Chan, C. K.: Particulate nitrate photolysis in the
541 atmosphere, *Environ. Sci. Atmos.*, [10.1039/D1EA00087J](https://doi.org/10.1039/D1EA00087J), 2022.
- 542 Gu, R., Shen, H., Xue, L., Wang, T., Gao, J., Li, H., Liang, Y., Xia, M., Yu, C., Liu, Y., and Wang,
543 W.: Investigating the sources of atmospheric nitrous acid (HONO) in the megacity of Beijing,
544 China, *Sci. Total Environ.*, 812, 152270, [10.1016/j.scitotenv.2021.152270](https://doi.org/10.1016/j.scitotenv.2021.152270), 2022a.
- 545 Gu, R., Wang, W., Peng, X., Xia, M., Zhao, M., Zhang, Y., Wang, Y. n., Liu, Y., Shen, H., Xue, L.,
546 Wang, T., and Wang, W.: Nitrous acid in the polluted coastal atmosphere of the South China
547 Sea: Ship emissions, budgets, and impacts, *Sci. Total Environ.*, 826, 153692,
548 [10.1016/j.scitotenv.2022.153692](https://doi.org/10.1016/j.scitotenv.2022.153692), 2022b.

549 Hao, Q., Jiang, N., Zhang, R., Yang, L., and Li, S.: Characteristics, sources, and reactions of nitrous
550 acid during winter at an urban site in the Central Plains Economic Region in China, *Atmos.*
551 *Chem. Phys.*, 20, 7087-7102, 10.5194/acp-20-7087-2020, 2020.

552 Harrison, R. M. and Kitto, A.-M. N.: Evidence for a surface source of atmospheric nitrous acid, *Atmos.*
553 *Environ.*, 28, 1089-1094, 10.1016/1352-2310(94)90286-0, 1994.

554 Jenkin, M. E., Young, J. C., and Rickard, A. R.: The MCM v3.3.1 degradation scheme for isoprene,
555 *Atmos. Chem. Phys.*, 15, 11433-11459, 10.5194/acp-15-11433-2015, 2015.

556 Jiang, Y., Xue, L., Shen, H., Dong, C., Xiao, Z., and Wang, W.: Dominant Processes of HONO Derived
557 from Multiple Field Observations in Contrasting Environments, *Environ. Sci. Technol. Lett.*,
558 9, 258-264, 10.1021/acs.estlett.2c00004, 2022.

559 Jiang, Y., Hoffmann, E. H., Tilgner, A., Aiyuk, M. B. E., Andersen, S. T., Wen, L., van Pinxteren, M.,
560 Shen, H., Xue, L., Wang, W., and Herrmann, H.: Insights into NO_x and HONO chemistry in
561 the tropical marine boundary layer at Cape Verde during the MarParCloud campaign, *J.*
562 *Geophys. Res. Atmos.*, 10.1029/2023jd038865, 2023.

563 Jiang, Y., Xue, L., Gu, R., Jia, M., Zhang, Y., Wen, L., Zheng, P., Chen, T., Li, H., Shan, Y., Zhao,
564 Y., Guo, Z., Bi, Y., Liu, H., Ding, A., Zhang, Q., and Wang, W.: Sources of nitrous acid
565 (HONO) in the upper boundary layer and lower free troposphere of the North China Plain:
566 insights from the Mount Tai Observatory, *Atmos. Chem. Phys.*, 20, 12115-12131,
567 10.5194/acp-20-12115-2020, 2020.

568 Kasibhatla, P., Sherwen, T., Evans, M. J., Carpenter, L. J., Reed, C., Alexander, B., Chen, Q. J.,
569 Sulprizio, M. P., Lee, J. D., Read, K. A., Bloss, W., Crilley, L. R., Keene, W. C., Pszenny, A.
570 A. P., and Hodzic, A.: Global impact of nitrate photolysis in sea-salt aerosol on NO_x, OH, and
571 O₃ in the marine boundary layer, *Atmos. Chem. Phys.*, 18, 11185-11203, 10.5194/acp-18-
572 11185-2018, 2018.

573 Kebede, M. A., Bish, D. L., Losovyj, Y., Engelhard, M. H., and Raff, J. D.: The Role of Iron-Bearing
574 Minerals in NO₂ to HONO Conversion on Soil Surfaces, *Environ. Sci. Technol.*, 50, 8649-
575 8660, 10.1021/acs.est.6b01915, 2016.

576 Kleffmann, J.: Daytime sources of nitrous acid (HONO) in the atmospheric boundary layer,
577 *Chemphyschem*, 8, 1137-1144, 10.1002/cphc.200700016, 2007.

578 Kleffmann, J., Becker, K., and Wiesen, P.: Heterogeneous NO₂ conversion processes on acid surfaces:
579 possible atmospheric implications, *Atmos. Environ.*, 32, 2721-2729, 1998.

580 Kleffmann, J., Kurtenbach, R., Lörzer, J., Wiesen, P., Kalthoff, N., Vogel, B., and Vogel, H.: Measured
581 and simulated vertical profiles of nitrous acid—Part I: Field measurements, *Atmos. Environ.*,
582 37, 2949-2955, 10.1016/s1352-2310(03)00242-5, 2003.

583 Kleffmann, J., Gavriloaiei, T., Hofzumahaus, A., Holland, F., Koppmann, R., Rupp, L., Schlosser, E.,
584 Siese, M., and Wahner, A.: Daytime formation of nitrous acid: A major source of OH radicals
585 in a forest, *Geophys. Res. Lett.*, 32, L05818, 10.1029/2005gl022524, 2005.

586 Kramer, L. J., Crilley, L. R., Adams, T. J., Ball, S. M., Pope, F. D., and Bloss, W. J.: Nitrous acid
587 (HONO) emissions under real-world driving conditions from vehicles in a UK road tunnel,
588 *Atmos. Chem. Phys.*, 20, 5231-5248, 10.5194/acp-20-5231-2020, 2020.

589 Kurtenbach, R., Becker, K. H., Gomes, J. A. G., Kleffmann, J., Lorzer, J. C., Spittler, M., Wiesen, P.,
590 Ackermann, R., Geyer, A., and Platt, U.: Investigations of emissions and heterogeneous
591 formation of HONO in a road traffic tunnel, *Atmos. Environ.*, 35, 3385-3394, 10.1016/s1352-
592 2310(01)00138-8, 2001.

593 Lee, J. D., Whalley, L. K., Heard, D. E., Stone, D., Dunmore, R. E., Hamilton, J. F., Young, D. E.,
594 Allan, J. D., Laufs, S., and Kleffmann, J.: Detailed budget analysis of HONO in central London
595 reveals a missing daytime source, *Atmos. Chem. Phys.*, 16, 2747-2764, 10.5194/acp-16-2747-
596 2016, 2016.

597 Lelièvre, S., Bedjanian, Y., Laverdet, G., and Le Bras, G.: Heterogeneous reaction of NO₂ with
598 hydrocarbon flame soot, *J. Phys. Chem. A*, 108, 10807-10817, 2004.

599 Li, D., Xue, L., Wen, L., Wang, X., Chen, T., Mellouki, A., Chen, J., and Wang, W.: Characteristics
600 and sources of nitrous acid in an urban atmosphere of northern China: Results from 1-yr
601 continuous observations, *Atmos. Environ.*, 182, 296-306, 10.1016/j.atmosenv.2018.03.033,
602 2018a.

603 Li, L., Duan, Z., Li, H., Zhu, C., Henkelman, G., Francisco, J. S., and Zeng, X. C.: Formation of HONO
604 from the NH₃-promoted hydrolysis of NO₂ dimers in the atmosphere, *P. Natl. Acad. Sci.*, 115,
605 7236-7241, 10.1073/pnas.1807719115, 2018b.

606 Li, M., Su, H., Li, G., Ma, N., Pöschl, U., and Cheng, Y.: Relative importance of gas uptake on aerosol
607 and ground surfaces characterized by equivalent uptake coefficients, *Atmos. Chem. Phys.*, 19,
608 10981-11011, 10.5194/acp-19-10981-2019, 2019.

609 Liao, S., Zhang, J., Yu, F., Zhu, M., Liu, J., Ou, J., Dong, H., Sha, Q., Zhong, Z., Xie, Y., Luo, H.,
610 Zhang, L., and Zheng, J.: High Gaseous Nitrous Acid (HONO) Emissions from Light-Duty
611 Diesel Vehicles, *Environ. Sci. Technol.*, 55, 200-208, 10.1021/acs.est.0c05599, 2021.

612 Liu, C.-M., Young, C.-Y., and Lee, Y.-C.: Influence of Asian dust storms on air quality in Taiwan,
613 *Sci. Total Environ.*, 368, 884-897, 10.1016/j.scitotenv.2006.03.039, 2006.

614 Liu, J., Li, S., Mekic, M., Jiang, H., Zhou, W., Loisel, G., Song, W., Wang, X., and Gligorovski, S.:
615 Photoenhanced Uptake of NO₂ and HONO Formation on Real Urban Grime, *Environ. Sci.*
616 *Technol. Lett.*, 6, 413-417, 10.1021/acs.estlett.9b00308, 2019a.

617 Liu, T. and Abbatt, J. P. D.: Oxidation of sulfur dioxide by nitrogen dioxide accelerated at the interface
618 of deliquesced aerosol particles, *Nat Chem*, 13, 1173-1177, 10.1038/s41557-021-00777-0,
619 2021.

620 Liu, Y., Shen, H., Mu, J., Li, H., Chen, T., Yang, J., Jiang, Y., Zhu, Y., Meng, H., Dong, C., Wang,
621 W., and Xue, L.: Formation of peroxyacetyl nitrate (PAN) and its impact on ozone production
622 in the coastal atmosphere of Qingdao, North China, *Sci. Total Environ.*, 778, 146265,
623 [10.1016/j.scitotenv.2021.146265](https://doi.org/10.1016/j.scitotenv.2021.146265), 2021.

624 Liu, Y. H., Lu, K. D., Li, X., Dong, H. B., Tan, Z. F., Wang, H. C., Zou, Q., Wu, Y. S., Zeng, L. M.,
625 Hu, M., Min, K. E., Kecorius, S., Wiedensohler, A., and Zhang, Y. H.: A Comprehensive
626 Model Test of the HONO Sources Constrained to Field Measurements at Rural North China
627 Plain, *Environ. Sci. Technol.*, 53, 3517-3525, 10.1021/acs.est.8b06367, 2019b.

628 Ma, Q., Wang, T., Liu, C., He, H., Wang, Z., Wang, W., and Liang, Y.: SO₂ Initiates the Efficient
629 Conversion of NO₂ to HONO on MgO Surface, *Environ Sci Technol*, 51, 3767-3775,
630 10.1021/acs.est.6b05724, 2017.

631 Meusel, H., Kuhn, U., Reiffs, A., Mallik, C., Harder, H., Martinez, M., Schuladen, J., Bohn, B.,
632 Parchatka, U., Crowley, J. N., Fischer, H., Tomsche, L., Novelli, A., Hoffmann, T., Janssen, R.
633 H. H., Hartogensis, O., Pikridas, M., Vrekoussis, M., Bourtsoukidis, E., Weber, B., Lelieveld,
634 J., Williams, J., Poschl, U., Cheng, Y. F., and Su, H.: Daytime formation of nitrous acid at a
635 coastal remote site in Cyprus indicating a common ground source of atmospheric HONO and
636 NO, *Atmos. Chem. Phys.*, 16, 14475-14493, 10.5194/acp-16-14475-2016, 2016.

637 Nie, W., Ding, A. J., Xie, Y. N., Xu, Z., Mao, H., Kerminen, V. M., Zheng, L. F., Qi, X. M., Huang,
638 X., Yang, X. Q., Sun, J. N., Herrmann, E., Petäjä, T., Kulmala, M., and Fu, C. B.: Influence of
639 biomass burning plumes on HONO chemistry in eastern China, *Atmos. Chem. Phys.*, 15, 1147-
640 1159, 10.5194/acp-15-1147-2015, 2015.

641 Reed, C., Evans, M. J., Crilley, L. R., Bloss, W. J., Sherwen, T., Read, K. A., Lee, J. D., and Carpenter,
642 L. J.: Evidence for renoxification in the tropical marine boundary layer, *Atmos. Chem. Phys.*,
643 17, 4081-4092, 10.5194/acp-17-4081-2017, 2017.

644 Romer, P. S., Wooldridge, P. J., Crouse, J. D., Kim, M. J., Wennberg, P. O., Dibb, J. E., Scheuer, E.,
645 Blake, D. R., Meinardi, S., Brosius, A. L., Thames, A. B., Miller, D. O., Brune, W. H., Hall, S.
646 R., Ryerson, T. B., and Cohen, R. C.: Constraints on Aerosol Nitrate Photolysis as a Potential
647 Source of HONO and NO_x, *Environ. Sci. Technol.*, 52, 13738-13746, 10.1021/acs.est.8b03861,
648 2018.

- 649 Shi, Q., Tao, Y., Krechmer, J. E., Heald, C. L., Murphy, J. G., Kroll, J. H., and Ye, Q.: Laboratory
650 Investigation of Renoxification from the Photolysis of Inorganic Particulate Nitrate, *Environ.*
651 *Sci. Technol.*, 55, 854-861, 10.1021/acs.est.0c06049, 2021.
- 652 Stemmler, K., Ammann, M., Donders, C., Kleffmann, J., and George, C.: Photosensitized reduction of
653 nitrogen dioxide on humic acid as a source of nitrous acid, *Nature*, 440, 195-198,
654 10.1038/nature04603, 2006.
- 655 Stemmler, K., Ndour, M., Elshorbany, Y., Kleffmann, J., D'Anna, B., George, C., Bohn, B., and
656 Ammann, M.: Light induced conversion of nitrogen dioxide into nitrous acid on submicron
657 humic acid aerosol, *Atmos. Chem. Phys.*, 7, 4237-4248, 10.5194/acp-7-4237-2007, 2007.
- 658 Su, H., Cheng, Y. F., Shao, M., Gao, D. F., Yu, Z. Y., Zeng, L. M., Slanina, J., Zhang, Y. H., and
659 Wiedensohler, A.: Nitrous acid (HONO) and its daytime sources at a rural site during the 2004
660 PRIDE-PRD experiment in China, *J. Geophys. Res. Atmos.*, 113, [10.1029/2007JD009060](https://doi.org/10.1029/2007JD009060),
661 2008.
- 662 Su, H., Cheng, Y., Oswald, R., Behrendt, T., Trebs, I., Meixner, F. X., Andreae, M. O., Cheng, P.,
663 Zhang, Y., and Poschl, U.: Soil nitrite as a source of atmospheric HONO and OH radicals,
664 *Science*, 333, 1616-1618, 10.1126/science.1207687, 2011.
- 665 Tang, Y., An, J., Wang, F., Li, Y., Qu, Y., Chen, Y., and Lin, J.: Impacts of an unknown daytime
666 HONO source on the mixing ratio and budget of HONO, and hydroxyl, hydroperoxyl, and
667 organic peroxy radicals, in the coastal regions of China, *Atmos. Chem. Phys.*, 15, 9381-9398,
668 10.5194/acp-15-9381-2015, 2015.
- 669 Theys, N., Volkamer, R., Müller, J. F., Zarzana, K. J., Kille, N., Clarisse, L., De Smedt, I., Lerot, C.,
670 Finkenzeller, H., Hendrick, F., Koenig, T. K., Lee, C. F., Knote, C., Yu, H., and Van
671 Roozendaal, M.: Global nitrous acid emissions and levels of regional oxidants enhanced by
672 wildfires, *Nat. Geosci.*, 13, 681-686, 10.1038/s41561-020-0637-7, 2020.
- 673 Tong, S., Hou, S., Zhang, Y., Chu, B., Liu, Y., He, H., Zhao, P., and Ge, M.: Exploring the nitrous
674 acid (HONO) formation mechanism in winter Beijing: direct emissions and heterogeneous
675 production in urban and suburban areas, *Faraday Discuss.*, 189, 213-230, 10.1039/c5fd00163c,
676 2016.
- 677 Underwood, G. M., Song, C. H., Phadnis, M., Carmichael, G. R., and Grassian, V. H.: Heterogeneous
678 reactions of NO₂ and HNO₃ on oxides and mineral dust: A combined laboratory and modeling
679 study, *J. Geophys. Res. Atmos.*, 106, 18055-18066, 10.1029/2000JD900552, 2001.
- 680 VandenBoer, T. C., Brown, S. S., Murphy, J. G., Keene, W. C., Young, C. J., Pszenny, A. A. P., Kim,
681 S., Warneke, C., de Gouw, J. A., Maben, J. R., Wagner, N. L., Riedel, T. P., Thornton, J. A.,
682 Wolfe, D. E., Dubé, W. P., Öztürk, F., Brock, C. A., Grossberg, N., Lefer, B., Lerner, B.,
683 Middlebrook, A. M., and Roberts, J. M.: Understanding the role of the ground surface in
684 HONO vertical structure: High resolution vertical profiles during NACHTT-11, *J. Geophys.*
685 *Res. Atmos.*, 118, 10,155-110,171, 10.1002/jgrd.50721, 2013.
- 686 Villena, G., Wiesen, P., Cantrell, C. A., Flocke, F., Fried, A., Hall, S. R., Hornbrook, R. S., Knapp, D.,
687 Kosciuch, E., Mauldin, R. L., McGrath, J. A., Montzka, D., Richter, D., Ullmann, K., Walega,
688 J., Weibring, P., Weinheimer, A., Staebler, R. M., Liao, J., Huey, L. G., and Kleffmann, J.:
689 Nitrous acid (HONO) during polar spring in Barrow, Alaska: A net source of OH radicals?, *J.*
690 *Geophys. Res.*, 116, D00R07, 10.1029/2011jd016643, 2011.
- 691 Vogel, B., Vogel, H., Kleffmann, J., and Kurtenbach, R.: Measured and simulated vertical profiles of
692 nitrous acid—Part II. Model simulations and indications for a photolytic source, *Atmos.*
693 *Environ.*, 37, 2957-2966, 10.1016/s1352-2310(03)00243-7, 2003.
- 694 Wang, S.: Atmospheric observations of enhanced NO₂-HONO conversion on mineral dust particles,
695 *Geophys. Res. Lett.*, 30, 10.1029/2003gl017014, 2003.
- 696 Wang, Y. Q.: MeteoInfo: GIS software for meteorological data visualization and analysis, *MeApp*, 21,
697 360-368, 10.1002/met.1345, 2012.

- 698 Wojtal, P., Halla, J. D., and McLaren, R.: Pseudo steady states of HONO measured in the nocturnal
699 marine boundary layer: a conceptual model for HONO formation on aqueous surfaces, *Atmos.*
700 *Chem. Phys.*, 11, 3243-3261, 10.5194/acp-11-3243-2011, 2011.
- 701 Wu, C., Zhang, S., Wang, G., Lv, S., Li, D., Liu, L., Li, J., Liu, S., Du, W., Meng, J., Qiao, L., Zhou,
702 M., Huang, C., and Wang, H.: Efficient Heterogeneous Formation of Ammonium Nitrate on
703 the Saline Mineral Particle Surface in the Atmosphere of East Asia during Dust Storm Periods,
704 *Environ. Sci. Technol.*, 54, 15622-15630, 10.1021/acs.est.0c04544, 2020.
- 705 Wurl, O., Stolle, C., Van Thuoc, C., The Thu, P., and Mari, X.: Biofilm-like properties of the sea
706 surface and predicted effects on air-sea CO₂ exchange, *Prog. Oceanogr.*, 144, 15-24,
707 10.1016/j.pocean.2016.03.002, 2016.
- 708 Xing, L., Wu, J., Elser, M., Tong, S., Liu, S., Li, X., Liu, L., Cao, J., Zhou, J., El-Haddad, I., Huang,
709 R., Ge, M., Tie, X., Prévôt, A. S. H., and Li, G.: Wintertime secondary organic aerosol
710 formation in Beijing–Tianjin–Hebei (BTH): contributions of HONO sources and
711 heterogeneous reactions, *Atmos. Chem. Phys.*, 19, 2343-2359, 10.5194/acp-19-2343-2019,
712 2019.
- 713 Xue, C., Ye, C., Kleffmann, J., Zhang, C., Catoire, V., Bao, F., Mellouki, A., Xue, L., Chen, J., Lu,
714 K., Zhao, Y., Liu, H., Guo, Z., and Mu, Y.: Atmospheric measurements at Mt. Tai—Part I:
715 HONO formation and its role in the oxidizing capacity of the upper boundary layer, *Atmos.*
716 *Chem. Phys.*, 22, 3149-3167, 10.5194/acp-22-3149-2022, 2022.
- 717 Xue, C., Zhang, C., Ye, C., Liu, P., Catoire, V., Krysztofiak, G., Chen, H., Ren, Y., Zhao, X., Wang,
718 J., Zhang, F., Zhang, C., Zhang, J., An, J., Wang, T., Chen, J., Kleffmann, J., Mellouki, A., and
719 Mu, Y.: HONO Budget and Its Role in Nitrate Formation in the Rural North China Plain,
720 *Environ. Sci. Technol.*, 54, 11048-11057, 10.1021/acs.est.0c01832, 2020a.
- 721 Xue, C. Y., Zhang, C. L., Ye, C., Liu, P. F., Catoire, V., Krysztofiak, G., Chen, H., Ren, Y. G., Zhao,
722 X. X., Wang, J. H., Zhang, F., Zhang, C. X., Zhang, J. W., An, J. L., Wang, T., Chen, J. M.,
723 Kleffmann, J., Mellouki, A., and Mu, Y. J.: HONO Budget and Its Role in Nitrate Formation
724 in the Rural North China Plain, *Environ. Sci. Technol.*, 54, 11048-11057,
725 10.1021/acs.est.0c01832, 2020b.
- 726 Xue, L. K., Wang, T., Gao, J., Ding, A. J., Zhou, X. H., Blake, D. R., Wang, X. F., Saunders, S. M.,
727 Fan, S. J., Zuo, H. C., Zhang, Q. Z., and Wang, W. X.: Ground-level ozone in four Chinese
728 cities: precursors, regional transport and heterogeneous processes, *Atmos. Chem. Phys.*, 14,
729 13175-13188, 10.5194/acp-14-13175-2014, 2014.
- 730 Yabushita, A., Enami, S., Sakamoto, Y., Kawasaki, M., Hoffmann, M., and Colussi, A.: Anion-
731 catalyzed dissolution of NO₂ on aqueous microdroplets, *J. Phys. Chem. A*, 113, 4844-4848,
732 2009.
- 733 Yang, J., Shen, H., Guo, M.-Z., Zhao, M., Jiang, Y., Chen, T., Liu, Y., Li, H., Zhu, Y., Meng, H.,
734 Wang, W., and Xue, L.: Strong marine-derived nitrous acid (HONO) production observed in
735 the coastal atmosphere of northern China, *Atmos. Environ.*, 244,
736 10.1016/j.atmosenv.2020.117948, 2021a.
- 737 Yang, X., Xue, L., Wang, T., Wang, X., Gao, J., Lee, S., Blake, D. R., Chai, F., and Wang, W.:
738 Observations and Explicit Modeling of Summertime Carbonyl Formation in Beijing:
739 Identification of Key Precursor Species and Their Impact on Atmospheric Oxidation Chemistry,
740 *J. Geophys. Res. Atmos.*, 123, 1426-1440, 10.1002/2017jd027403, 2018.
- 741 Yang, Y., Li, X., Zu, K., Lian, C., Chen, S., Dong, H., Feng, M., Liu, H., Liu, J., Lu, K., Lu, S., Ma,
742 X., Song, D., Wang, W., Yang, S., Yang, X., Yu, X., Zhu, Y., Zeng, L., Tan, Q., and Zhang,
743 Y.: Elucidating the effect of HONO on O₃ pollution by a case study in southwest China, *Sci.*
744 *Total Environ.*, 756, 144127, 10.1016/j.scitotenv.2020.144127, 2021b.
- 745 Ye, C., Zhang, N., Gao, H., and Zhou, X.: Photolysis of Particulate Nitrate as a Source of HONO and
746 NO_x, *Environ. Sci. Technol.*, 51, 6849-6856, 10.1021/acs.est.7b00387, 2017.

747 Ye, C., Zhou, X., Pu, D., Stutz, J., Festa, J., Spolaor, M., Tsai, C., Cantrell, C., Mauldin, R. L., 3rd,
748 Campos, T., Weinheimer, A., Hornbrook, R. S., Apel, E. C., Guenther, A., Kaser, L., Yuan, B.,
749 Karl, T., Haggerty, J., Hall, S., Ullmann, K., Smith, J. N., Ortega, J., and Knote, C.: Rapid
750 cycling of reactive nitrogen in the marine boundary layer, *Nature*, 532, 489-491,
751 10.1038/nature17195, 2016a.

752 Ye, C. X., Gao, H. L., Zhang, N., and Zhou, X. L.: Photolysis of Nitric Acid and Nitrate on Natural
753 and Artificial Surfaces, *Environ. Sci. Technol.*, 50, 3530-3536, 10.1021/acs.est.5b05032,
754 2016b.

755 Yu, C., Wang, Z., Ma, Q., Xue, L., George, C., and Wang, T.: Measurement of heterogeneous uptake
756 of NO₂ on inorganic particles, sea water and urban grime, *J. Environ. Sci.*, 106, 124-135,
757 [10.1016/j.jes.2021.01.018](https://doi.org/10.1016/j.jes.2021.01.018), 2021.

758 Yu, C., Huang, L., Xue, L., Shen, H., Li, Z., Zhao, M., Yang, J., Zhang, Y., Li, H., Mu, J., and Wang,
759 W.: Photoenhanced Heterogeneous Uptake of NO₂ and HONO Formation on Authentic Winter
760 Time Urban Grime, *ACS Earth Space Chem.*, 6, 1960-1968,
761 10.1021/acsearthspacechem.2c00054, 2022a.

762 Yu, Y., Cheng, P., Li, H., Yang, W., Han, B., Song, W., Hu, W., Wang, X., Yuan, B., Shao, M., Huang,
763 Z., Li, Z., Zheng, J., Wang, H., and Yu, X.: Budget of nitrous acid (HONO) at an urban site in
764 the fall season of Guangzhou, China, *Atmos. Chem. Phys.*, 22, 8951-8971, 10.5194/acp-22-
765 8951-2022, 2022b.

766 Zha, Q. Z., Xue, L. K., Wang, T., Xu, Z., Yeung, C. P., Louie, P. K. K., and Luk, C. W. Y.: Large
767 conversion rates of NO₂ to HNO₂ observed in air masses from the South China Sea: Evidence
768 of strong production at sea surface?, *Geophys. Res. Lett.*, 41, 7710-7715,
769 10.1002/2014gl061429, 2014.

770 Zhang, Q., Liu, P., Wang, Y., George, C., Chen, T., Ma, S., Ren, Y., Mu, Y., Song, M., Herrmann, H.,
771 Mellouki, A., Chen, J., Yue, Y., Zhao, X., Wang, S., and Zeng, Y.: Unveiling the
772 underestimated direct emissions of nitrous acid (HONO), *P. Natl. Acad. Sci.*, 120,
773 e2302048120, 10.1073/pnas.2302048120, 2023.

774 Zhang, R., Gen, M., Huang, D., Li, Y., and Chan, C. K.: Enhanced Sulfate Production by Nitrate
775 Photolysis in the Presence of Halide Ions in Atmospheric Particles, *Environ. Sci. Technol.*, 54,
776 3831-3839, 10.1021/acs.est.9b06445, 2020.

777 Zhang, W., Tong, S., Ge, M., An, J., Shi, Z., Hou, S., Xia, K., Qu, Y., Zhang, H., Chu, B., Sun, Y.,
778 and He, H.: Variations and sources of nitrous acid (HONO) during a severe pollution episode
779 in Beijing in winter 2016, *Sci. Total Environ.*, 648, 253-262, 10.1016/j.scitotenv.2018.08.133,
780 2019.

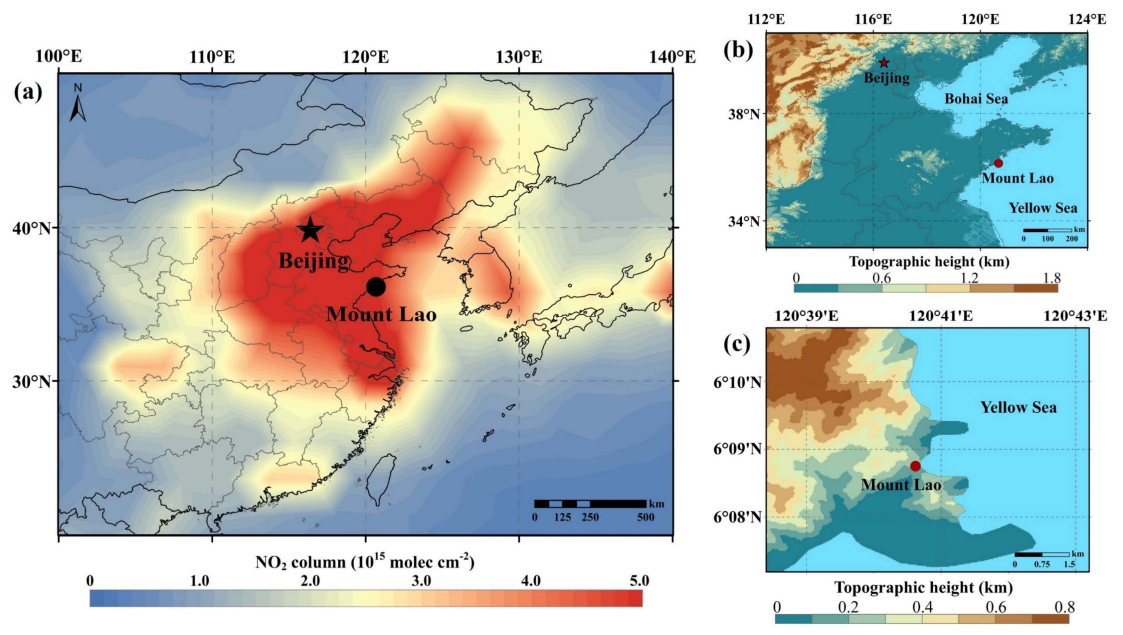
781 Zhang, X., Tong, S., Jia, C., Zhang, W., Li, J., Wang, W., Sun, Y., Wang, X., Wang, L., Ji, D., Wang,
782 L., Zhao, P., Tang, G., Xin, J., Li, A., and Ge, M.: The Levels and Sources of Nitrous Acid
783 (HONO) in Winter of Beijing and Sanmenxia, *J. Geophys. Res. Atmos.*, 127,
784 10.1029/2021jd036278, 2022.

785 Zhou, X., Zhang, N., TerAvest, M., Tang, D., Hou, J., Bertman, S., Alaghmand, M., Shepson, P. B.,
786 Carroll, M. A., Griffith, S., Dusanter, S., and Stevens, P. S.: Nitric acid photolysis on forest
787 canopy surface as a source for tropospheric nitrous acid, *Nat. Geosci.*, 4, 440-443,
788 10.1038/ngeo1164, 2011.

789 Zhou, X. L., Gao, H. L., He, Y., Huang, G., Bertman, S. B., Civerolo, K., and Schwab, J.: Nitric acid
790 photolysis on surfaces in low-NO_x environments: Significant atmospheric implications,
791 *Geophys. Res. Lett.*, 30, 10.1029/2003gl018620, 2003.

792 Zhu, Y., Wang, Y., Zhou, X., Elshorbany, Y. F., Ye, C., Hayden, M., and Peters, A. J.: An investigation
793 into the chemistry of HONO in the marine boundary layer at Tudor Hill Marine Atmospheric
794 Observatory in Bermuda, *Atmos. Chem. Phys.*, 22, 6327-6346, 10.5194/acp-22-6327-2022,
795 2022.

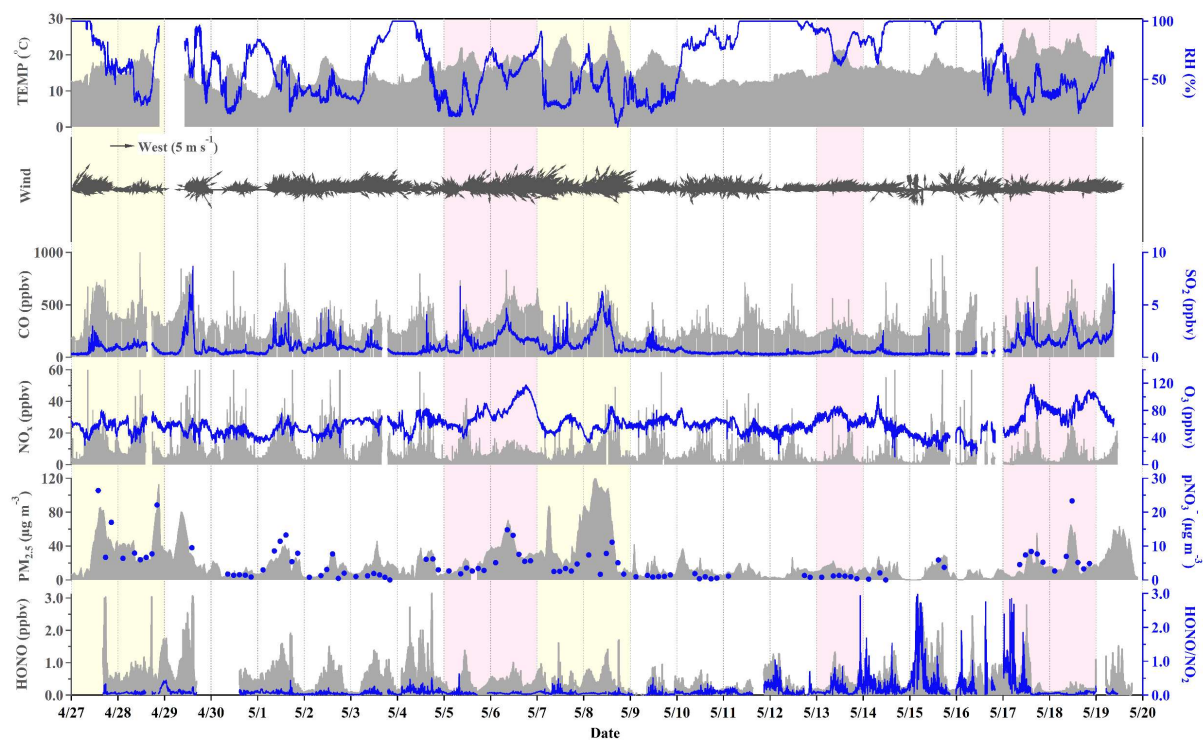
796



799

800 **Figure 1.** Maps showing the location of the monitoring site. Figure 1a is colored by tropospheric NO₂
801 column density in May 2021 from the Ozone Monitoring Instrument (OMI,
802 <https://www.earthdata.nasa.gov/>), and Figure 1b and Figure 1c are colored by the geographical height
803 from the Geospatial Data Cloud (<http://www.gscloud.cn/>).

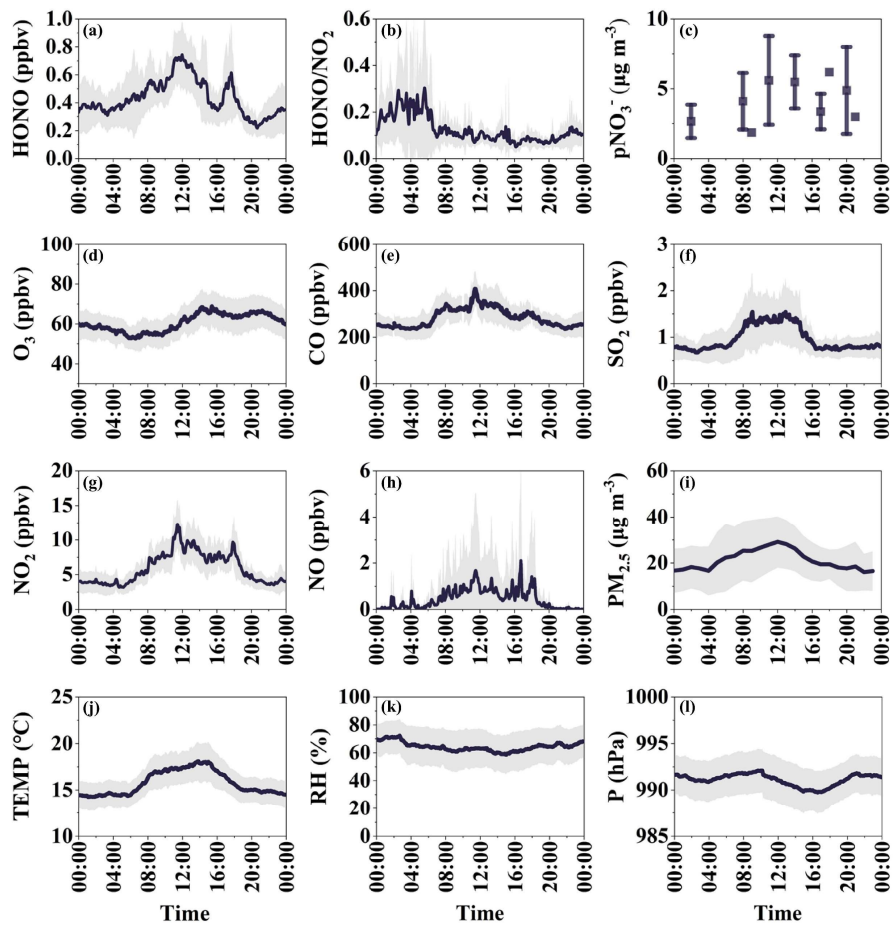
804



805

806 **Figure 2.** Time series of HONO, meteorological parameters, and related species measured during the
 807 campaign. The yellow shaded areas correspond to the period of dust, while the pink shaded areas
 808 represent the period of photochemical pollution.

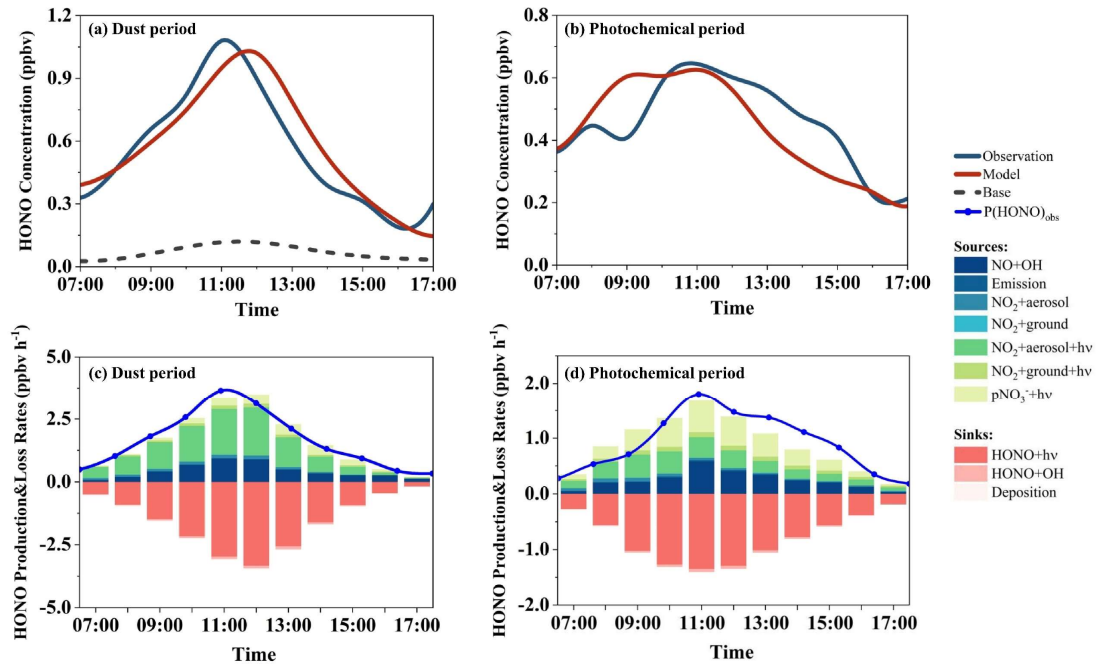
809



810

811 **Figure 3.** Average diurnal variations of (a) HONO, (b) HONO/NO₂, (c) particle nitrate, (d) O₃, (e) CO,
 812 (f) SO₂, (g) NO₂, (h) NO, (i) PM_{2.5}, (j) temperature, (k) RH, and (l) pressure during the observation
 813 period. The shaded area indicates the range of half of the standard deviation.

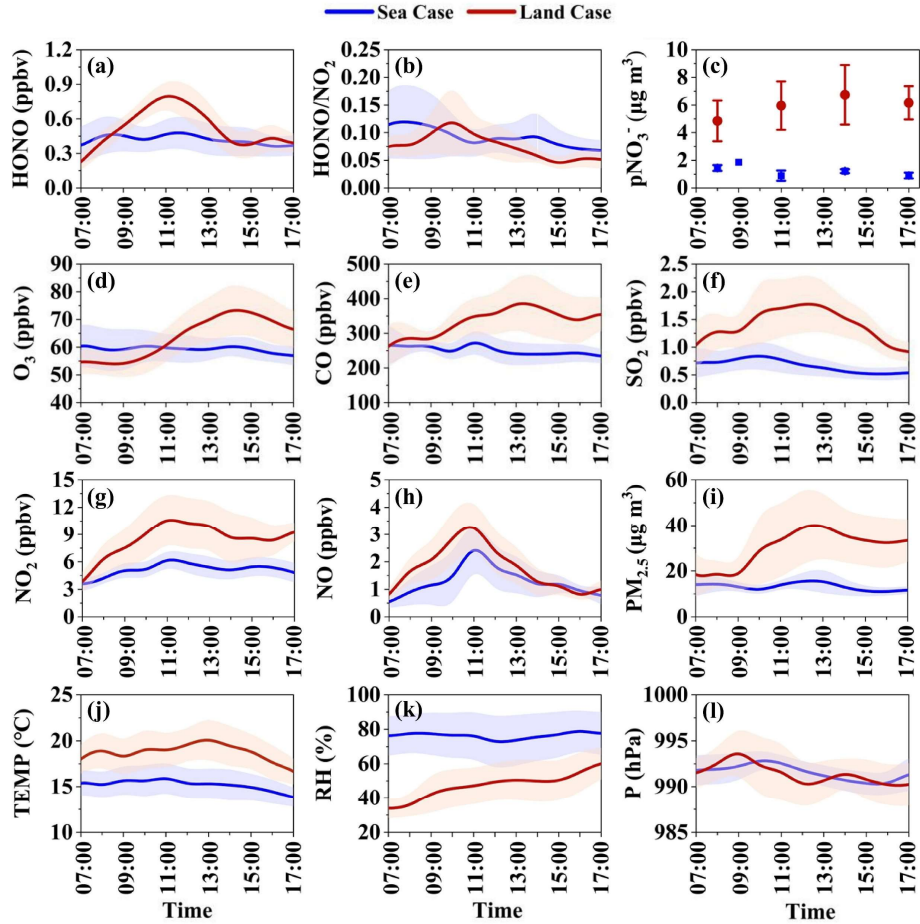
814



815

816 **Figure 4.** Daytime HONO budgets in dust (a, c) and (b, d) photochemical period at Mount Lao. The
 817 base case only considered the homogeneous reaction of $\text{NO} + \text{OH}$, and the model case considered the
 818 updated HONO sources described in this study.

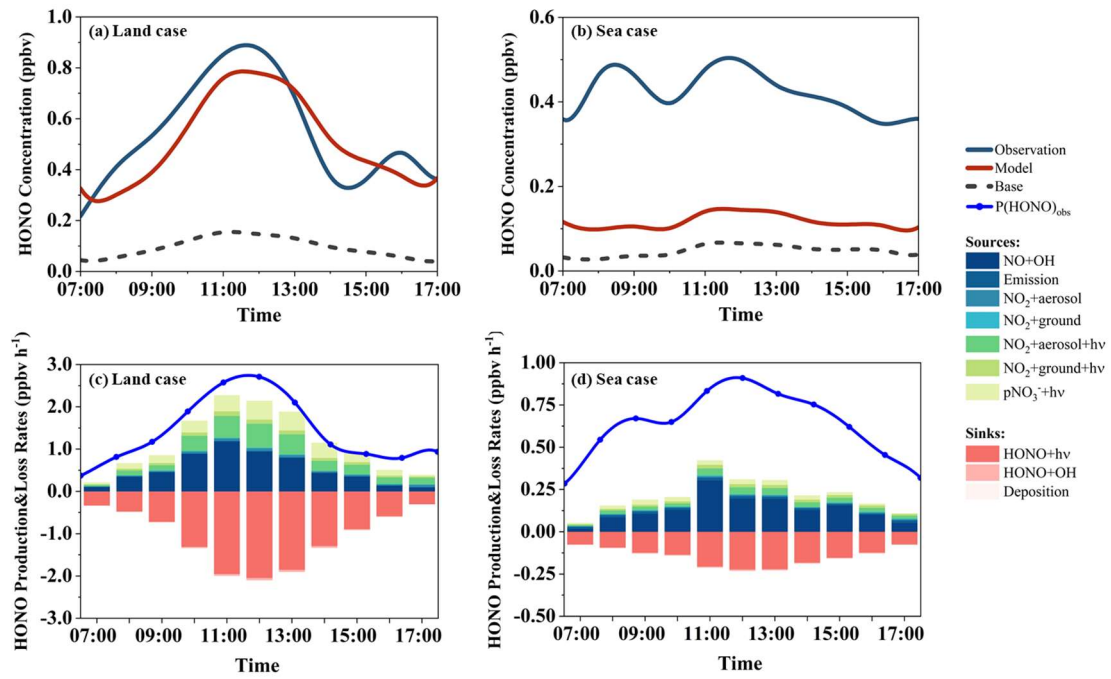
819



820

821 **Figure 5.** Average diurnal variations of HONO and related parameters in the “sea case” and the “land
 822 case” during the campaign at Mount Lao. The shaded area indicates half of the standard deviation.

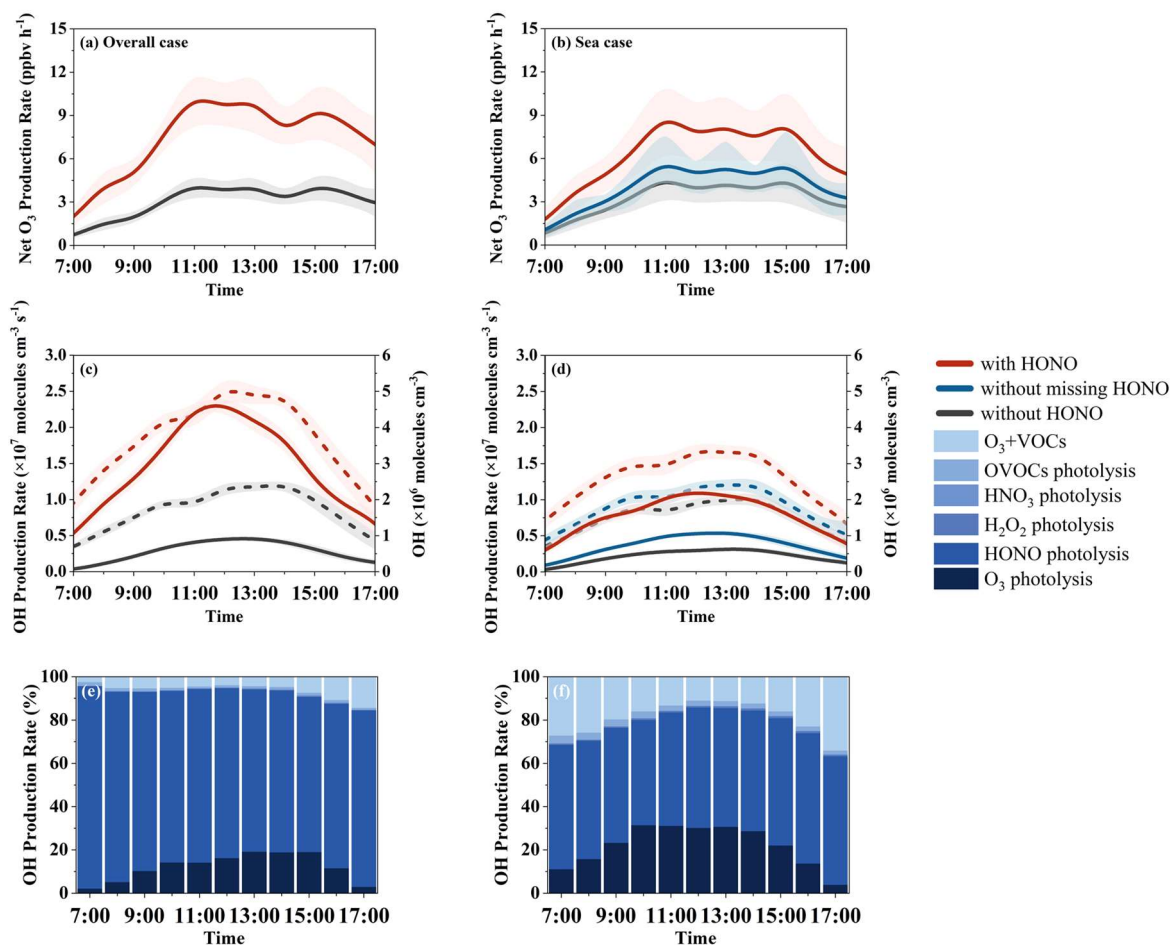
823



824

825 **Figure 6.** Comparison of the observed and modeled daytime (7:00–17:00) HONO concentrations and
 826 modeled HONO budgets in the “land case” (a, c) and the “sea case” (b, d).

827



828

829 **Figure 7.** Comparison of simulated net O₃ and OH radical production rate (solid lines) and
 830 concentration (dashed lines) with and without HONO measurement data constraints and relative
 831 diurnal contributions of different OH radical sources with HONO constrained in the “land case” (a, c,
 832 e) and the “sea case” (b, d, f). The shaded area indicates the standard deviation.

833

834 **Table 1.** Summary of HONO source and sinks included in the box model.

Pathways	Parametrization	References
Direct emission	$k_{\text{emission}} = 0.8\%$	Kleffmann et al. (2003)
$\text{OH} + \text{NO} \rightarrow \text{HONO}$	$k_{\text{OH+NO}}$	Calculated in model
$\text{NO}_2 + \text{H}_2\text{O} \xrightarrow{\text{aerosol surface}} \text{HONO} + \text{HNO}_3$	$k = 0.25 \times v_{\text{NO}_2} \times \text{Sa} \times \gamma_a$ $\gamma_a = 8 \times 10^{-6}$	Vandenboer et al. (2013)
$\text{NO}_2 + \text{H}_2\text{O} \xrightarrow{\text{ground surface}} \text{HONO} + \text{HNO}_3$	$k = 0.25 \times v_{\text{NO}_2} \times \gamma_g \times \frac{S}{V}$ $\gamma_g = 1 \times 10^{-6}, \frac{S}{V} = \frac{1.7}{\text{BLH}}$	Kleffmann et al. (1998); Vogel et al. (2003)
$\text{NO}_2 + h\nu \xrightarrow{\text{aerosol surface}} \text{HONO}$	$k = 0.25 \times v_{\text{NO}_2} \times \text{Sa} \times \gamma_{a, h\nu} \times \frac{J_{\text{NO}_2}}{J_{\text{NO}_2, \text{noon}}}$ $\gamma_{a, h\nu} = 4 \times 10^{-5}$	Lelièvre et al. (2004)
$\text{NO}_2 + h\nu \xrightarrow{\text{ground surface}} \text{HONO}$	$k = 0.25 \times v_{\text{NO}_2} \times \gamma_{g, h\nu} \times \frac{S}{V} \times \frac{J_{\text{NO}_2}}{J_{\text{NO}_2, \text{noon}}}$ $\gamma_{g, h\nu} = 2 \times 10^{-5}, \frac{S}{V} = \frac{1.7}{\text{BLH}}$	Stemmler et al. (2006); Vogel et al. (2003)
$\text{pNO}_3^- + h\nu \rightarrow \text{HONO}$	$k = \frac{8.3 \times 10^{-5}}{7 \times 10^{-7}} \times J(\text{HNO}_3)_{\text{MCM}}$	Ye et al. (2017)
$\text{HONO} + h\nu \rightarrow \text{NO} + \text{OH}$	$k = J(\text{HONO})$	Calculated in model
$\text{HONO} + \text{OH} \rightarrow \text{H}_2\text{O} + \text{NO}_2$	$k_{\text{OH+HONO}}$	Calculated in model
Deposition	$k = \frac{v_{\text{HONO}}}{\text{BLH}}$	Calculated in model

835

836 **Table 2.** Statistics of measured species and meteorological parameters during the campaign.

Parameters	Mean	SD	Minimum	Median	Maximum
HONO (ppbv)	0.46	0.37	< DL (0.005)	0.38	3.14
HONO/NO ₂	0.13	0.24	–	0.07	2.97
NO (ppbv)	0.9	1.7	0.1	0.2	38.3
NO ₂ (ppbv)	5.9	4.8	0.4	4.6	65.1
O ₃ (ppbv)	60.4	15.8	11.6	58.8	118.1
CO (ppbv)	284.0	118.8	104.2	250.3	1046.7
SO ₂ (ppbv)	1.0	0.8	< DL (0.12)	0.7	8.9
PM _{2.5} (µg m ⁻³)	21.2	21.0	< DL (0.5)	14.4	120.7
Sa (m ² m ⁻³)	6.2×10 ⁻⁴	5.8×10 ⁻⁴	2.8×10 ⁻⁴	4.2×10 ⁻⁴	3.1×10 ⁻³
pNO ₃ ⁻ (µg m ⁻³)	4.6	5.0	0.02*	2.8	26.4
TEMP (°C)	15.1	3.4	7.5	15.6	27.9
RH (%)	68.7	26.1	9.0	64.8	99.9
P (kPa)	991.1	4.4	979.0	991.0	1003.0
WS (m s ⁻¹)	1.23	0.96	0*	1.00	9.30
WD (°)	–	–	0	247	354

837 DL: detection limit.

838

839 **Table 3.** Comparison of the statistics for the measured species and meteorological parameters during
 840 dust, photochemical pollution, and non-polluted periods in the daytime (7:00–17:00).

Parameters	Dust period	Photochemical period	Non-polluted period
HONO (ppbv)	0.57 ± 0.39	0.44 ± 0.29	0.40 ± 0.34
HONO/NO ₂	0.07 ± 0.04	0.10 ± 0.13	0.10 ± 0.12
NO (ppbv)	1.8 ± 1.8	1.2 ± 1.4	1.8 ± 2.0
NO ₂ (ppbv)	9.8 ± 5.0	7.1 ± 4.4	7.1 ± 4.6
O ₃ (ppbv)	58.0 ± 10.8	78.8 ± 17.3	54.9 ± 11.7
CO (ppbv)	371.8 ± 151.9	353.8 ± 117.5	277.6 ± 98.0
SO ₂ (ppbv)	1.6 ± 1.3	1.7 ± 0.8	0.7 ± 0.6
PM _{2.5} (μg m ⁻³)	45.4 ± 32.3	25.0 ± 17.4	17.2 ± 12.6
PM ₁₀ (μg m ⁻³)	235.3 ± 200.8	68.0 ± 47.2	32.8 ± 21.8
Sa (m ² m ⁻³)	$1.28 \times 10^{-3} \pm 8.41 \times 10^{-4}$	$6.81 \times 10^{-4} \pm 4.73 \times 10^{-4}$	$5.58 \times 10^{-4} \pm 4.22 \times 10^{-4}$
pNO ₃ ⁻ (μg m ⁻³)	7.0 ± 6.2	6.2 ± 5.6	3.0 ± 3.4
TEMP (°C)	19.0 ± 3.4	20.5 ± 2.7	15.1 ± 2.4
RH (%)	47.8 ± 24.7	47.4 ± 17.2	71.6 ± 27.0
WS (m s ⁻¹)	0.42 ± 0.35	0.65 ± 0.33	0.38 ± 0.25
JNO ₂ (s ⁻¹)	$6.6 \times 10^{-3} \pm 2.2 \times 10^{-3}$	$7.0 \times 10^{-3} \pm 2.1 \times 10^{-3}$	$4.5 \times 10^{-3} \pm 2.2 \times 10^{-3}$

841